nanomaterials

MDPI

Review

g-C_3N_4: Properties, Pore Modifications, and Photocatalytic Applications

Jiaqi Dong [1,†], Yue Zhang [2,†], Muhammad Irfan Hussain [1], Wenjie Zhou [2], Yingzhi Chen [1,2,*] and Lu-Ning Wang [1,2,*]

[1] School of Materials Science and Engineering, University of Science and Technology Beijing, Beijing 100083, China; 13691129766@163.com (J.D.); irfanustb@163.com (M.I.H.)
[2] Shunde Graduate School, University of Science and Technology Beijing, Foshan 528399, China; 13126595311@163.com (Y.Z.); zhouwenjie1459@163.com (W.Z.)
* Correspondence: chenyingzhi@ustb.edu.cn (Y.C.); luning.wang@ustb.edu.cn (L.-N.W.)
† These authors equally contributed to this work.

Abstract: Graphitic carbon nitride (g-C_3N_4), as a polymeric semiconductor, is promising for ecological and economical photocatalytic applications because of its suitable electronic structures, together with the low cost, facile preparation, and metal-free feature. By modifying porous g-C_3N_4, its photoelectric behaviors could be facilitated with transport channels for photogenerated carriers, reactive substances, and abundant active sites for redox reactions, thus further improving photocatalytic performance. There are three types of methods to modify the pore structure of g-C_3N_4: hard-template method, soft-template method, and template-free method. Among them, the hard-template method may produce uniform and tunable pores, but requires toxic and environmentally hazardous chemicals to remove the template. In comparison, the soft templates could be removed at high temperatures during the preparation process without any additional steps. However, the soft-template method cannot strictly control the size and morphology of the pores, so prepared samples are not as orderly as the hard-template method. The template-free method does not involve any template, and the pore structure can be formed by designing precursors and exfoliation from bulk g-C_3N_4 (BCN). Without template support, there was no significant improvement in specific surface area (SSA). In this review, we first demonstrate the impact of pore structure on photoelectric performance. We then discuss pore modification methods, emphasizing comparison of their advantages and disadvantages. Each method's changing trend and development direction is also summarized in combination with the commonly used functional modification methods. Furthermore, we introduce the application prospects of porous g-C_3N_4 in the subsequent studies. Overall, porous g-C_3N_4 as an excellent photocatalyst has a huge development space in photocatalysis in the future.

Keywords: g-C_3N_4; pore structure; template method; template-free method; photocatalysis

Citation: Dong, J.; Zhang, Y.; Hussain, M.I.; Zhou, W.; Chen, Y.; Wang, L.-N. g-C_3N_4: Properties, Pore Modifications, and Photocatalytic Applications. *Nanomaterials* **2022**, *12*, 121. https://doi.org/10.3390/nano12010121

Academic Editor: Vincenzo Vaiano

Received: 13 November 2021
Accepted: 24 December 2021
Published: 30 December 2021

1. Introduction

In the last few decades, energy shortage and environmental remediation have become serious challenges to the long-term development of humanity. As an advanced green technology, semiconductor-based photocatalysis takes inexhaustible solar light as a driving force and a suitable semiconductor as a catalyst to cause photogenerated electrons and holes, and hence conducts photoredox reactions. Inorganic semiconductors (ISCs) are a group of widely used photocatalysts, such as TiO_2, SnO_2, ZnO, etc., which have the advantages of a high concentration of free charge carriers and high carrier mobility, and high physical and chemical stability [1]. However, they are usually limited by the narrow and fixed absorption spectrum [2], and the structural modification usually involves complicated fabrication processes or harsh conditions [3]. Compared with ISCs, organic semiconductors (OSCs) are characterized by structural diversity and synthetic functionality, and thus have easily tunable photoelectronic properties via structure/property engineering.

In the OSC family, conjugated polymers, *g*-C_3N_4 [4–8], polypyrrole (PPy) [9,10], polyaniline (PANI) [11,12], polyimide (PI) [13], poly (3-hexylthiophene) (P3HT) [14], polyhydroxybutyrate (PHB) [15,16], etc., have been extensively used for photocatalytic purposes due to their broad, molecular-level tuning of optoelectronic properties. Among them, *g*-C_3N_4 resembles graphene and has a unique two-dimensional (2D) delocalized conjugated structure, which is formed by an infinite extension of triazine ring (C_3N_3) or tri-s-triazine ring (C_6N_7) as basic structural units [17]. Such structural features endow *g*-C_3N_4 with relatively larger SSA and hence more active sites for charge separation and redox reaction than other polymer semiconductors. In addition, the strong covalent bond between the triazine ring in *g*-C_3N_4 leads to extraordinary chemical and thermal stability (up to 600 °C) compared to other polymorphs, and this stability is the highest in organic materials. Moreover, *g*-C_3N_4 has the moderate bandgap (E_g) of 2.7 eV, as well as a conduction band (CB) and valence band (VB) position at −1.4 eV and 1.3 eV (vs. normal hydrogen electrode (NHE)), respectively, which could meet various redox reaction potentials by easily engineering its structure [18]. Therefore, *g*-C_3N_4 has found ample possibilities in different photocatalytic application fields, mainly including overall water splitting [19–21], CO_2 reduction [22–24], degradation of organic pollutants [25], and antibacterial [26–29].

Despite these advantages, *g*-C_3N_4 still suffers from some drawbacks, such as narrow visible light response (~450 nm) and rapid recombination of photogenerated carriers, which limit their photocatalytic performance [30]. Numerous works have emerged to remedy the issues by applying second materials, such as doping metals [31,32] and nonmetals [33,34], or combining with other semiconductors [35,36], adsorptive materials [37], and photosensitizers [38]. In addition, diverse synthetic pathways to obtain *g*-C_3N_4 structure have been employed in previous reports, for example, physical [39] or chemical vapor deposition [25,40], solvothermal method [41–43], solid-state reaction [44], and thermal nitridation [45]. Among the above strategies, thermal condensation of several low-cost nitrogen-rich precursors is facile and the most commonly used method. Figure 1 shows the thermal condensation process to prepare *g*-C_3N_4 from different precursors, including cyanamide [46], dicyanamide [47], melamine [48], urea [49], and thiourea [50]. However, the SSA of BCN is still limited for enhancing their photocatalytic performance. It has been demonstrated that morphology and porosity control of pristine *g*-C_3N_4 could help achieve higher SSA and a high number of active sites for improving optical absorption and prolonging the lifetime of the photogenerated charge carriers. Modifying the pore structure of *g*-C_3N_4 appears to be an effective way to improve the optoelectronic properties and photocatalytic performance. Regarding the pores, it is generally assumed that micropores (<2 nm) have the smallest pore size and thus the largest SSA, which allows them to have more active sites to absorb particles, such as electrons and ions. Mesopores (2–50 nm) are more conducive to the transport of reactants or solvents because they have a shorter void distance between pores. Besides, multiple light reflection inside mesopores enhances light utilization efficiency. Macropores (>50 nm) have better adsorption of organic macromolecule or gas molecules for their removal and product transportation. From there, pore size control toward a good balance between light absorption, reactant adsorption, and charge/mass transport is essential to high photon-to-electron conversion efficiency.

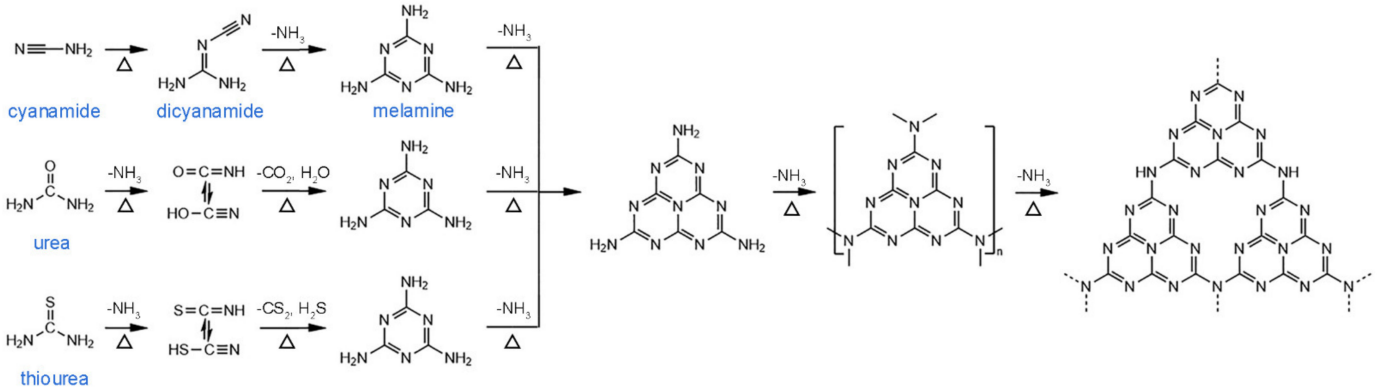

Figure 1. Thermal condensation process to prepare *g*-C_3N_4 from different precursors: cyanamide, dicyanamide, melamine, urea, and thiourea.

Pore modification methods of *g*-C_3N_4 can be generally categorized into three types: hard-template method [51–54], soft-template method [55–59], and template-free method [60–63] (Figure 2). Hard template provides good support in yielding relatively regular pores that can act as a good channel for the migration of photogenerated charge. While the experimental operation process is relatively complicated because the templates must require an additional removal process. Soft-template method mainly introduces templates with diverse morphologies and can be easily decomposed during the condensation of *g*-C_3N_4. The template-free method does not involve any templates, which simplifies the experimental process to the greatest extent and reduces the cost. Using these methods, it is possible to control the pore volume, pore size, and SSA of the prepared porous *g*-C_3N_4 to modify the optoelectronic properties and photocatalytic function.

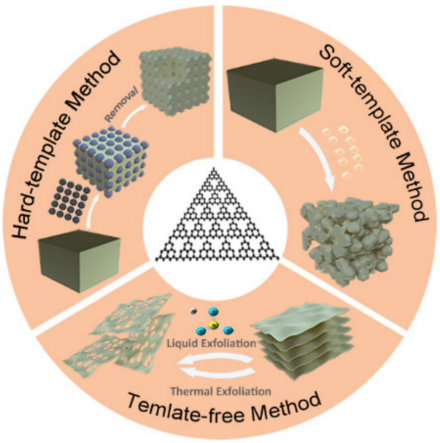

Figure 2. Pore modification methods over *g*-C_3N_4: hard-template method, soft-template method, template-free method.

In this review, the pore structure-dependent properties are first introduced. Furthermore, we discuss three pore modification methods (hard-template method, soft-template method, template-free method) with their advantages and disadvantages, highlighting the effects of pore structure on the photoelectric properties and photocatalytic performance. Recent achievements of pore structure *g*-C_3N_4 in photocatalytic fields, including water splitting, CO_2 reduction, and wastewater treatment, are then introduced. Finally, some challenges and prospects for the future development of porous *g*-C_3N_4-based photocatalysts are proposed.

2. Pore Structure/Properties Relationship

The pore structure in the material has a great influence on its electrochemical properties [64–68]. As discussed early, micro- and mesopores are important in creating a large accessible surface and interface areas for charge carrier generation, transfer, and transport, and macropores are favorable for mass transport.

Microporous materials have the smallest pore size and could attain the largest SSA, allowing them to expose more active sites to electrons and ions. Numerous studies have revealed that the micropores are crucial in activating O_2 and other small molecules, such as H_2O, by absorbing more electrons and ions. A microporous graphitic carbon with strictly regular porosity and diameter of 0.63–0.97 nm, has demonstrated ultra-high SSA of 1927.6 $m^2 \cdot g^{-1}$, giving a photocatalytic H_2 evolution rate of 58.3 $\mu mol \cdot h^{-1} \cdot g^{-1}$ [69]. Metal-organic frameworks (MOFs), well known as porous coordination polymers, have been considered as ideal precursors for well-designed semiconductors with microporous structures. For example, Fe-based MOFs Fe-MIL-100 with a pore size of ~2 nm exhibited an SSA of 1203.36 $m^2 \cdot g^{-1}$, yielding a tetracycline (TC) degradation constant of 9×10^{-3} [70]. However, Fe-MIL-101 with a larger pore (25.74 nm) and lower SSA showed better photocatalytic performance (1.63×10^{-2}). On one hand, the more micropores, the larger the SSA materials will get. On the other hand, the relationship between SSA and properties is not always positive. Because the void distance of micropores will be relatively longer, which is not conducive to the diffusion of reactants and the occurrence of reaction in terms of kinetics. Therefore, there is rare literature on microporous *g*-C_3N_4 in photocatalysis.

As for mesoporous materials, their pore size is larger than that of micropores materials and smaller than that of macropores materials. Generally, suppose the porous material is used as the catalyst carrier. In that case, the active metals are generally distributed in the microporous part, and the larger metal particles will be in the mesoporous. Compared with micropores materials, mesoporous are more conducive to the transport of reactants or solvents because they have a shorter void distance between pores. For example, Tian et al., presented a three-dimensional (3D) ultrathin mesoporous N doped *g*-C_3N_4 (UM3) with urea and melamine as precursors [71]. UM3 possessed the highest SSA (39.1 $m^2 \cdot g^{-1}$) with a pore diameter of 46.1 nm among all the samples. The UV-vis diffuse reflectance spectrometry (DRS) showed that UM3 has the lowest E_g of 2.47 eV, while BCNs is 2.70 eV. The narrower E_g allowed UM3 to increase the utilization ability of the solar spectrum. As for the result, the UM3 yielded an H_2 evolution rate of 3579 $\mu mol \cdot h^{-1} \cdot g^{-1}$, which was almost 23 times higher than that of BCN (147 $\mu mol \cdot h^{-1} \cdot g^{-1}$).

On the other hand, macropores materials have better adsorption for liquids with high viscosity. However, the pore size of macropores is too large for ordinary reactants or solvents. Therefore, the pure macropores materials are not very practical. They can be useful for exposure to other kinds of pores [72]. In general, if a material has these three kinds of pores simultaneously, it can integrate the characteristics of the three kinds of pores materials and be more effective in its application. These types of materials are called hierarchically porous materials [73,74]. Li et al., synthesized macroscopic foam-like holey ultrathin *g*-C_3N_4 nanosheets (CNHS) with micro-, meso-, and macropores by thermal polycondensation of melamine [75]. The SSA of CNHS and BCN are 227.98 and 10.89 $m^2 \cdot g^{-1}$, respectively. Notably, the macropores in CNHS accounted for the maximum ratio of 52.1% for the total volume. Still, they accounted for the minimum ratio of 16.8% for SSA, while the mesopores in CNHS accounted for 46.7% of the total volume and the maximum ratio of 57.8% for the SSA. This meant that the macropores mainly serve for the exposure of the mesopores. As for the optical properties, the DRS showed a slight blue shift of the intrinsic absorption edge of CNHS. The E_g of the CNHS was 2.81 eV, larger than that of the BCN (2.70 eV). This may lead to a larger thermodynamic driving force in photocatalytic H_2 evolution. Consequently, the H_2 evolution rate of CNHS was 57.20 $\mu mol \cdot h^{-1}$, which was over 22 times larger than that of BCN. Herein, most of the porous *g*-C_3N_4 used are micropores, mesoporous, micro/mesoporous, or meso/microporous [76–80]. Similarly, Wei et al., prepared macropores (500–700 nm) and mesopores (2–20 nm) Zr-based

MOF $Zr_6O_4(OH)_4(BDC)_{12}$ (UiO-66) to form advanced CdS/UiO-66 catalysts [81]. They found that the pore size impacted the spatial distribution of CdS nanoparticles: CdS tended to deposit on the external surface of mesoporous UiO-66, but spontaneously penetrated the large cavity of macroporous UiO-66 nanocage. By loading CdS, the photocatalytic reaction constant of macroporous CdS/UiO-66 over 4-nitroaniline reduction was three times higher than that of the mesoporous counterpart.

3. Pore Modifications over *g*-C_3N_4

3.1. Hard-Template Method

During hard-template method, the templates are mixed and coated with the precursors of *g*-C_3N_4 to generate pore structures according to the morphology of the templates. The existence of the templates provides good support for the sample. It makes the sample form a relatively regular pore structure, which provides good channels for the transmission of photoelectric charge. SiO_2 nanostructure and SiO_2 derivatives are mainly used in the hard-template method, which must be prepared in advance and removed by chemical reagents after the sample is formed [82–84]. The directly acquired salt templates simplify the experiment process, and importantly they could be removed with eco-friendly reagents.

3.1.1. SiO_2 as Template

Many studies have shown that a zero-dimensional (0D) SiO_2 nanostructure is widely used as a hard template. For one, SiO_2 has stable properties and suitable hardness, providing good support for samples. Second, the nanostructure of SiO_2 is regular and fine-tunable. Therefore, pores of *g*-C_3N_4 are ordered in shape and tunable in diameter along with SiO_2 in different sizes. Li et al., successfully synthesized porous C_3N_4 with dicyandiamide (DCDA) as precursors and SiO_2 nanoparticles (SiO_2 NPs) (7–40 nm) as hard templates [85]. In this study, DCDA and SiO_2 were dispersed with deionized water and dried to obtain a solid mixture. Then, the solid mixture was calcined to obtain *g*-C_3N_4 containing SiO_2. Finally, the sample was treated with 20% HF for four hours to obtain porous *g*-C_3N_4. The as-prepared samples had mesopores (5–40 nm) and a larger SSA of 109 $m^2 \cdot g^{-1}$, which was nearly 10 times of the BCN (11.89 $m^2 \cdot g^{-1}$). The larger SSA brought by the more porous structure increased the adsorption of RhB. The photocatalytic rhodamine B (RhB) degradation efficiency of porous C_3N4 (100%, in 30 min) was higher than that of the BCN (62%, in 30 min) [86]. However, the pore size of *g*-C_3N_4 was non-uniform due to the replication of multisize SiO_2, so there was no significant enhancement of light absorption.

The narrow scale range and appropriate content of SiO_2 is important to the regularity of pore structure. In an example, SiO_2 nanospheres with uniform size (~12 nm) were used as a hard template, which was mixed into precursor aminonitrile to prepare mesoporous *g*-C_3N_4 (MCN) [87]. According to the amounts of SiO_2 (0.625, 1.25, 2.5, 5.0, and 10 g), the as-prepared samples were denoted as MCN_r. The average pore sizes were uniformly near 12 nm for all samples, which could be regarded as a replica of the structure of the SiO_2 spheres. Compared with BCN (9 $m^2 \cdot g^{-1}$), the SSA of MCN_r was significantly improved (23–191 $m^2 \cdot g^{-1}$). When a large amount of the template was applied, the speculation that stackable small C_3N_4 pieces could be formed, resulting in destroying the pore structure, was proved in the sharply decreased total pore volume of $MCN_{4.0}$ (0.05 $cm^3 \cdot g^{-1}$) for other MCN_r. Among all the samples, $MCN_{1.0}$ had the largest SSA of ~191 $m^2 \cdot g^{-1}$ and total pore volume of ~0.52 $cm^3 \cdot g^{-1}$, respectively, which were 21.8 and 13.0-fold higher than that of BCN, respectively (Figure 3a). Due to the presence of regular mesopores and nanoscale pore walls, $MCN_{1.0}$ photoelectric performance was remarkably improved. For one reason, $MCN_{1.0}$ exhibited an upshift in the 400–600 nm for intensified light absorption (Figure 3b). Besides, charge separation of $MCN_{1.0}$ also was enhanced, as proved by the highest photocurrent intensity (4.11 $\mu A \cdot cm^{-2}$), 4.0 times of BCN (1.03 $\mu A \cdot cm^{-2}$) (Figure 3c). Therefore, the reaction rate constant for photocatalytic U(VI) reduction in $MCN_{1.0}$ (0.27 min^{-1}) was 6.75 times that of BCN (0.04 min^{-1}) (Figure 3d).

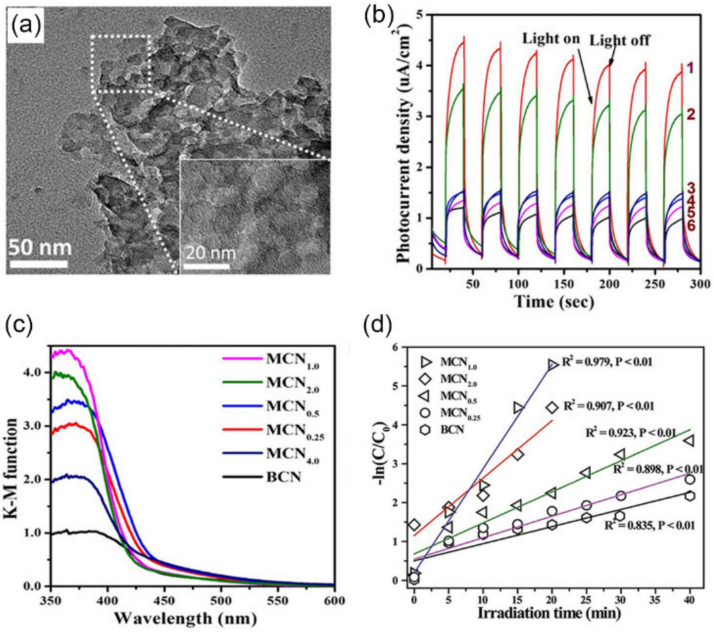

Figure 3. (**a**) Transmission electron microscope (TEM) images of $MCN_{1.0}$; (**b**) photocurrent responses spectra of as-synthesized BCN and MCN_r samples (the numbers on each line correspond to 1: $MCN_{1.0}$; 2: $MCN_{2.0}$; 3: $MCN_{4.0}$; 4: $MCN_{0.5}$; 5: $MCN_{0.25}$; and 6: BCN); (**c**) UV-vis DRS and (**d**) the rate constant for photocatalytic U(VI) reduction in BCN and MCN_r photocatalysts. Reprinted with permission from [87]. 2020 Elsevier.

3.1.2. SiO_2 Derivatives as Templates

In addition to SiO_2 nanostructures, some SiO_2 derivatives with intrinsic pore structures are developed as hard templates, such as santa barbara amorphous-15 (SBA-15) [88–93], mesocellular silica foam (MCF) [94], fibrous silica (KCC-1) [95], mesoporous silica (MCM-41) [96]. Due to the regulated pore diameter, these hard templates were applied to synthesize highly ordered and large SSA mesoporous *g*-C_3N_4.

As the morphology of *g*-C_3N_4 depends on the initial silica matrices due to the peculiarities of the replication process, spherical mesostructured *g*-C_3N_4 could be obtained with 3D sponge-like foam MCF or nanospherical silica KCC-1. In one case, carbon nitride (CN) spheres with a uniform diameter (~4 μm) in size had a well-defined 3D foam mesopore structure by replicating spherical silica MCFs [97]. Such spherical CN materials possessed small (4 nm) and large mesopores (43 nm), a high SSA of ~550 $m^2 \cdot g^{-1}$, and a pore volume of 0.90 $cm^3 \cdot g^{-1}$. Through downsizing the template to a nanoscale, porous *g*-C_3N_4 nanostructure could be generated. For example, fibrous silica KCC-1 nanospheres were used as a template, yielding nanospherical *g*-C_3N_4 (NS-*g*-C_3N_4) by thermal-induced self-polymerization of cyanamide molecules [98]. After removing the template by NH_4HF_2, NS-*g*-C_3N_4 with a diameter of ~200 nm was faithfully replicated by the spherical morphologies of KCC-1 (Figure 4a). Besides, well-defined 2D sheets of KCC-1 supported the formation of interconnected 2D *g*-C_3N_4 nanosheets. The distribution of polymeric nanosheets endowed NS-*g*-C_3N_4 with a mesoporous structure (pore size: ~20 nm), featuring an SSA of 160 $m^2 \cdot g^{-1}$. Due to the multiple reflections of incident light within mesoporous architectures, the light-harvesting ability of NS-*g*-C_3N_4 was greatly enhanced to 590 nm from 450 nm of BCN. A similar structure-induced property change was demonstrated in charge transportation. 3D interconnecting nanosheets could significantly shorten the diffusion length of charge migration and promote electron re-localization on surface terminal sites. Therefore, the charge recombination was suppressed, as proven by strong photoluminescence (PL) quench (Figure 4b). The enhanced photocurrent could further suggest the improved charge separation (inset in Figure 4b). Therefore, NS-*g*-C_3N_4 exhibited

a much-improved H_2 evolution rate (574 μmol·h^{-1}), far exceeding that of bulk-*g*-C_3N_4 (12.5 μmol·h^{-1}) (Figure 4c).

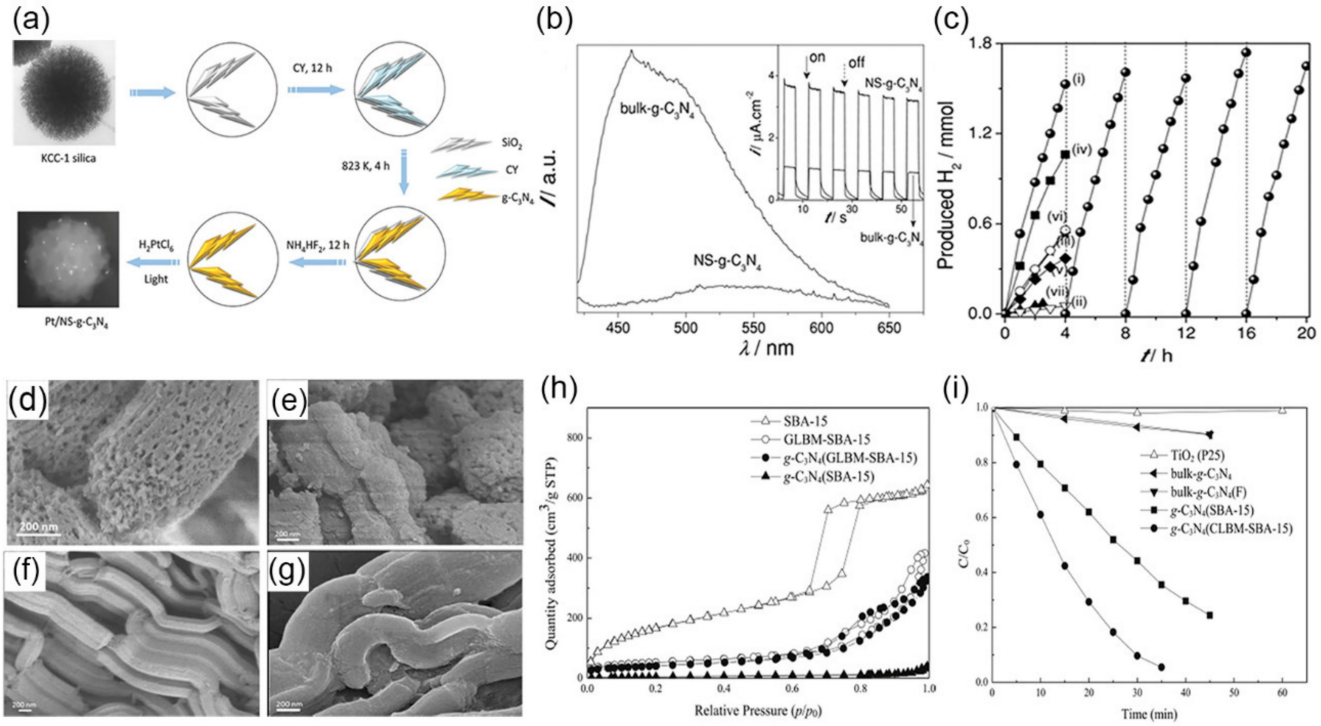

Figure 4. (**a**) Synthesis process of NS-*g*-C_3N_4; (**b**) PL spectra and photocurrent generation performance (inset) of NS-*g*-C_3N_4 and BCN; (**c**) Photocatalytic H2 evolution performance on (i) NS-*g*-C3N4, (ii) BCN, (iii) mesoporous *g*-C3N4, (iv) *g*-C3N4 hollow nanospheres, (v) *g*-C3N4 nanosheets, (vi) NS-*g*-C3N4 deformed by vigorous stirring in NH4HF2, (vii) NS-*g*-C3N4 deformed by grinding [98].; Scanning electron microscope (SEM) images of (**d**) CLBM-SBA-15, (**e**) *g*-C_3N_4(CLBM-SBA-15), (**f**) SBA-15, and (**g**) *g*-C_3N_4(SBA-15); (**h**) pore size distribution curves for SBA-15, *g*-C_3N_4(CLBM-SBA-15), *g*-C_3N_4(SBA-15), and CLBM-SBA-15; (**i**) photodegradation of MO on various *g*-C_3N_4 samples, Reprinted with permission from [83] 2015 Elsevier.

Among mesoporous silica templates, well-ordered hexagonal SBA-15 exhibits uniform pore sizes (~30 nm) and large SSA (843 m^2·g^{-1}), which is a good choice to regulate pore distribution and enlarge SSA of *g*-C_3N_4 [99]. For example, a mesoporous CN prepared by SBA-15 as hard templates could achieve a superhigh SSA of 788 m^2·g^{-1} and a large pore volume of 0.69 cm^3·g^{-1} [100]. The conventional SBA-15 is synthesized by hydrothermal treatment in acidic media [101]. In one work, SBA-15 was first obtained using Pluronic P123 and tetraethyl orthosilicate in HCl solution under 150 °C heat treatment [102]. Then, by using this SBA-15, *g*-C_3N_4 with mesopore (~5.3 nm) was prepared, giving an SSA of 239 m^2·g^{-1} and a pore volume of 0.34 cm^3·g^{-1}. The H_2 evolution on the mesoporous *g*-C_3N_4 (~85 μmol·h^{-1}) was about five times higher than BCN. Larger pore openings were essential for filling precursors to ensure complete replication of the pore structure of SBA-15. For example, researchers prepared a cross-linked bimodal SBA-15 (CLBM-SBA-15) with a larger pore opening size (44 nm) by decreasing the pH of the reaction solution to 7.5 [83]. Then, the mesoporous *g*-C_3N_4 samples were obtained by calcining the mixture of CLBM-SBA-15 or SBA-15 and precursor cyanamide. After that, the templates were removed with NH_4HF_2 solution, denoting the samples as *g*-C_3N_4(CLBM-SBA-15) or *g*-C_3N_4(SBA-15) (Figure 4d–g). Owing to the numerous pore openings of CLBM-SBA-15, *g*-C_3N_4(CLBM-SBA-15) had a pore size of 11–90 nm and a pore volume of 0.43 cm^3·g^{-1}. Compared to BCN and *g*-C_3N_4(SBA-15), *g*-C_3N_4(CLBM-SBA-15) had the largest SSA (145 m^2·g^{-1}), almost 8.5 and 20 times of *g*-C_3N_4(SBA-15) (17 m^2·g^{-1}) and BCN (7 m^2·g^{-1}), respectively (Figure 4h).

The formation of the mesoporous structure could provide more surface-active sites for photocatalytic process and be helpful to the adsorption of organic compounds. Therefore, methyl orange (MO) degradation rate of *g*-C_3N_4(CLBM-SBA-15) reached 15.3 μg·min^{-1}, which was 15.3 and 2 times than that of BCN and *g*-C_3N_4(SBA-15), respectively (Figure 4i).

3.1.3. Salt as Templates

In recent years, several studies on using metal salts (e.g., $Na_2S_2O_3$ [103], NaCl [104,105], KCl [106,107], $ZnCl_2$ [108]) as hard templates have appeared. These salts are easily acquired, which could simplify the preparation process. During this method, the solid salts are dissolved with precursors in the solution, and then the solvent is removed by rotary evaporation or freeze-drying, yielding a powder mixture. After the calcination of a mixture, the samples were added into hydrochloric acid or deionized water for template removing, which is environmentally friendly. In one case, 3D porous foam-like *g*-C_3N_4 (F-C_3N_4) was prepared by thermal polycondensation of melamine with NaCl as templates (Figure 5a) [104]. F-C_3N_4 bared a macropore-dominated hierarchically porous structure (pore size-range of 0.1–1 μm, centered at 60 nm) with an SSA of 50.3 $m^2 \cdot g^{-1}$, which was 12-fold of BCN (4.2 $m^2 \cdot g^{-1}$). Electrochemical impedance spectroscopy (EIS) plots showed that the arc radius of F-C_3N_4 (~151 kΩ) was smaller than that of pristine *g*-C_3N_4 (~191 kΩ), indicating its higher separation efficiency of electron-hole pairs and charge transfer ability. Great adsorption ability to tetracycline molecules of macropores also facilitated the photocatalytic process, as it was observed that the removal efficiency of TC by F-C_3N_4 was 5.65% in the dark, while there was no obvious adsorption of TC by BCN. Thanks to the synthetic effect, 99.7% TC was degraded by F-C_3N_4 after light irradiation, and only 4.22% TC was removed by BCN (Figure 5b).

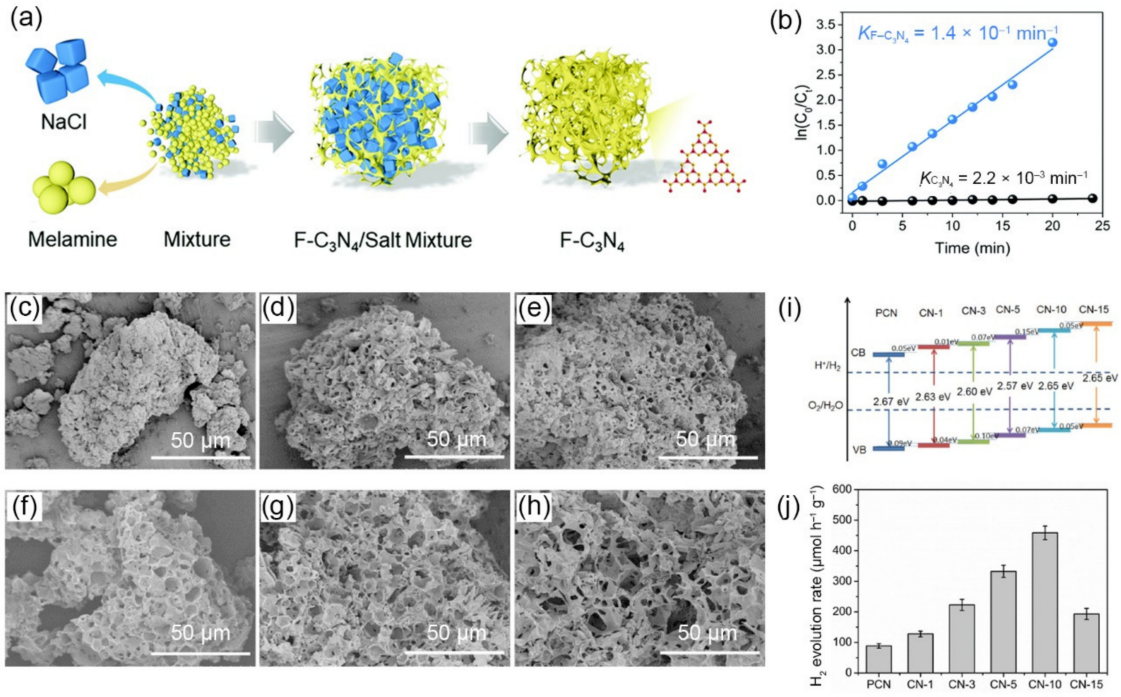

Figure 5. (**a**) Synthesis process of F-C_3N_4 by using melamine as precursor and NaCl as a template; (**b**) kinetic linear fitting curves of F-C_3N_4 and BCN, Reprinted with permission from [104]. 2020 Royal Society of Chemistry; (**c**) SEM images of CN, (**d**) CN-1, (**e**) CN-3, (**f**) CN-5, (**g**) CN-10, and (**h**) CN-15; (**i**) band structure and (**j**) photocatalytic H_2 evolution rate of PCN and CN-xs, Reprinted with permission from [109]. 2019 Elsevier.

As a hard template, the number of added salts plays an important role in adjusting photoelectric properties by tuning the pore structure of *g*-C_3N_4. Besides, metal salts

will cause element doing (e.g., Na^+, K^+, O) on porous *g*-C_3N_4 during heat treatment, influencing its band structure. For instance, Yang et al., fabricated a macrostructure *g*-C_3N_4 (pore size in a range of several hundred nanometers to several micrometers) through one-step calcination by using DCDA as a precursor and water-soluble NaCl cubes as the template, named CN-x (x, the molar ratio of NaCl/DCDA) [109]. After calcination, samples were washed with deionized water several times to remove the template. SEM images (Figure 5c–h) showed that the pore morphology of CN-x varied as the molar ratio of NaCl/DCDA changed. With the increment mass of NaCl, the number of holes was increased, and the size became larger, giving the higher SSA (up to 16.71 $m^2 \cdot g^{-1}$ of CN-10). When adding NaCl, the pore wall got thin because of closely assembled NaCl cubes, which destroyed the pore structure, leading to the decrease in SSA (11.23 $m^2 \cdot g^{-1}$ of CN-15). Except for pore modification, the introduction of salt caused Na^+ doping, influencing band structure of CN-x samples, as proved by the VB and CB in XPS results (Figure 5i). Owing to high SSA and suitable band structure, CN-10 exhibited the best photocatalytic H_2 evolution activity (459 $\mu mol \cdot h^{-1} \cdot g^{-1}$), about 5.2-fold of its bulk counterpart (Figure 5j).

In preparing photocatalyst experiments, the main role of a hard template is to construct and stabilize the pore structure. The pore structure can provide a channel for the transport of photogenerated electrons, promote the separation of electrons and holes, inhibit the recombination of electrons and holes, and thus enhance photocatalytic activity. Using SiO_2 as hard templates can ensure the regularity of pore structure. Porous SiO_2 derivative templates of different shapes endow *g*-C_3N_4 corresponding morphology, highly ordered pore distribution, as well as high SSA. However, the removal of SiO_2 requires toxic and harmful etchants, such as HF or NH_4HF_2, which will do harm to the environment. Although using salt as a hard template can simplify the experiments without template prefabrication and avoid the usage of pollutant reagents, removing the hard template is still needed. Herein, researchers were seeking other convenient ways to produce pore structure in *g*-C_3N_4.

3.2. Soft-Template Method

The soft-template method is a facile and effective way to produce high surface area [46]. This method mainly introduces templates that can be removed with high temperature in the preparation process. The selection of soft templates is more varied than that of hard templates, and the morphology is diverse, including the various surfactants and bubble templates. Besides, some precursors can be directly used as soft templates. The key is that these soft templates would be dissolved or released during heat treatment, so the separate steps to remove the template are no longer needed [110].

3.2.1. Surfactants as Templates

Surfactants are applied as a surface agent to the precursors, which form pores by their decomposition during thermal condensation of the precursors. This method requires that the surfactants have certain thermal and chemical stability in case of ahead decomposing. Besides, surfactant templates should be easily and completely decomposed to avoid affecting the electrical conductivity of *g*-C_3N_4. Commonly used surfactant soft templates include nonionic surfactants (e.g., Pluronic P-123 [111,112], Triton X-100 [46,113–115], Pluronic F-127 [116]) and ionic liquid [117–119].

The assistance of nonionic surfactants as soft templates has improved the surface area and porosity of *g*-C_3N_4. A study has shown that mesoporous CN synthesized with Pluronic F-127, Pluronic P-123, and Triton X-100 reached higher SSA (145, 164, and 186 $m^2 \cdot g^{-1}$) than that of BCN (10 $m^2 \cdot g^{-1}$) [120]. In addition, their pore volume was 0.51, 0.55, and 0.6 $cm^3 \cdot g^{-1}$, far exceeding that of BNC (less than 0.1 $cm^3 \cdot g^{-1}$). It was demonstrated that ionic liquid, consisting of a hydrophilic ionic head group and a hydrophobic organic chain, can self-assemble into micelles like surfactants in the aqueous solution, which have been widely used to induce the porous materials [121]. Such a strategy can also be involved to construct porous structure *g*-C_3N_4 photocatalysts. The benchmark performance of urea tended to grow around the micelles due to the weak hydrogen bonding with ionic liquids (1-

butyl-3-vinylimidazolium bromide) [122]. Meanwhile, the ionic liquid micelles could act as the center of the nucleation and growth of the *g*-C_3N_4 nanosheets. Thus, porous structures (pore size: ~85 nm) consisting of *g*-C_3N_4 nanosheets were prepared by the decomposing of ionic liquid micelles during the condensation of urea at a high temperature (Figure 6a), denoted pCN-X (X: the additive amount of ionic liquid). The calculated SSA and pore volume were 149.6 $m^2 \cdot g^{-1}$ and 0.796 $cm^3 \cdot g^{-1}$, respectively, which was about 3.6 and 4.6 times higher than those of pure CN (41.2 $m^2 \cdot g^{-1}$, 0.17 $cm^3 \cdot g^{-1}$). Owing to the multiple reflections of incident light within the porous structure, the pCN showed an extended light absorption in the range of 410–720 nm compared to 200–409 nm of BCN (Figure 6b). An outstanding H_2 evolution rate (120 $\mu mol \cdot h^{-1}$) was achieved, about 3.6 times higher than BCN (Figure 6c).

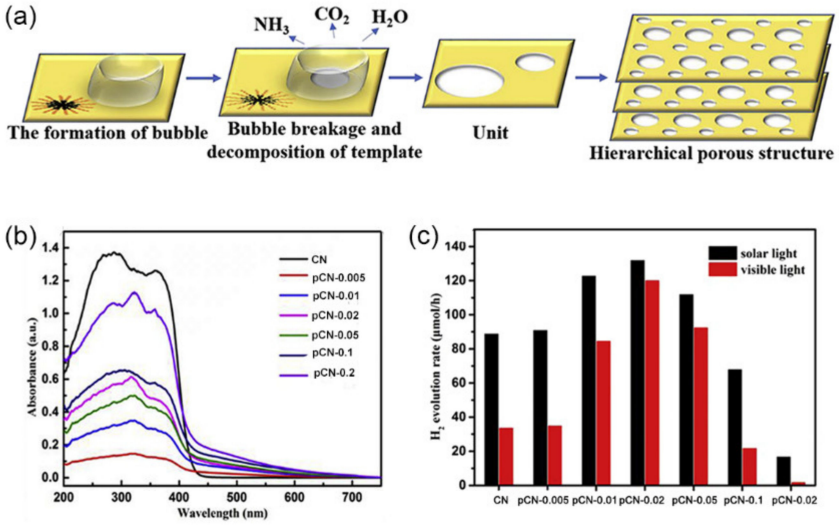

Figure 6. (**a**) Formation mechanism of highly porous pCN-X; (**b**) UV-vis DRS of CN and pCN-X (X = 0.005, 0.01, 0.02, 0.05, 0.1, 0.2); (**c**) photocatalytic H_2 evolution rate of pCN-X under solar and visible light irradiation ($\lambda \geq 400$ nm), Reprinted with permission from [122] 2017 Elsevier.

The choice of the precursor is important because the interaction between the precursor and the template affects the degree of polymerization [120]. The strong interaction between the surfactant molecule and precursors causes incomplete condensation of the precursor and the high level of carbon residue. The heavily doping contents would offer more potential recombination sites of the semiconductors, reducing their photocatalytic performance. When using Pluronic P123 as a template and DCDA as a precursor, a mesoporous *g*-C_3N_4 yielded disordered pore systems and a high molar ratio of C/N (0.82–2.06) because of the strong hydrogen bonds between PEO blocks of Pluronic P123 and DCDA [46]. In general, the heavily carbon contents would offer more potential recombination sites of the semiconductors, which have a negative effect on the improvement of photocatalytic performance. Considering melamine is a less reactive precursor than DCDA, Yan et al., used melamine as a precursor and Pluronic P123 surfactant as a soft template to avoid the direct chemical reaction between them, giving worm-like mesoporous *g*-C_3N_4 (pore size: ~20 nm) [123]. During thermal treatment, CN polymerization and surfactant combustion were independent, so that prepared *g*-C_3N_4 had a minor amount of carbon dopants (C/N: 0.69) and possessed a higher SSA of 90 $m^2 \cdot g^{-1}$ (10 times that of pristine *g*-C_3N_4). Therefore, the sufficient light absorption extended to the maximum of the solar spectrum (up to 800 nm), which played an important role to enhance photocatalytic H_2 evolution rate (148.2 $\mu mol \cdot h^{-1}$) with respect to the sample synthesized without using the surfactant (60.5 $\mu mol \cdot h^{-1}$).

3.2.2. Bubbles as Templates

Bubble template refers to the gases released by the decomposition of pore modifiers, which can promote the formation of porous structures during the calcination of the precursor. A kind of bubble template, such as H_2O and CO_2, only helps with supporting holes and has no effect on the precursor molecule itself. A sucrose-mediated *g*-C_3N_4 with small mesopores (2.3–3.5 nm) formed by H_2O and CO_2 released from sucrose had an SSA of 121 $m^2 \cdot g^{-1}$, and showed an optimal H_2 evolution rate of 107.8 $\mu mol \cdot h^{-1}$, which was 8.6 times higher than that of pristine *g*-C_3N_4 [124]. Similarly, using H_2O and CO_2 generated by acetic acid as a pore-forming template, the mesoporous *g*-C_3N_4 (pore size: 5–50 nm) with an SSA of 138 $m^2 \cdot g^{-1}$ had 13.75-times higher RhB degradation rate (2.2 $mg \cdot L^{-1} \cdot min^{-1}$) compared to BCN (0.16 $mg \cdot L^{-1} \cdot min^{-1}$) [125].

The inorganic ammonium salts (e.g., $NHCl_4$, NH_4HCO_3) can decompose to produce the thermal gas flow to leave pores, and the generated gases, such as NH_3 and HCl, would etch the s-triazine network structures, thus effectively promoting the production of pores and SSA. For example, taking NH_4Cl as a bubble template and melamine as the precursor, mesoporous *g*-C_3N_4 (mp*g*-C_3N_4) with a pore size of ~13.9 nm exhibited 12-times higher SSA (195 $m^2 \cdot g^{-1}$) and 5-times higher pore volume (0.627 $cm^3 \cdot g^{-1}$) compared to BCN (17 $m^2 \cdot g^{-1}$; 0.127 $cm^3 \cdot g^{-1}$) (Figure 7a) [126]. Such extraordinarily higher SSA provided more potential reaction sites and channels for mass transfer to participate in photocatalytic reactions. Furthermore, the mesoporous *g*-C_3N_4 framework geometrically shortened the diffusion length of the photogenerated charge carriers to the surface, leading to a suppressed photogenerated charge recombination, as proved by a much weaker PL peak intensity (Figure 7b). This could contribute to the enhanced photocatalytic chemical reaction. As a result, the mp*g*-C_3N_4 sample exhibited the higher photodegradation activity for RhB (100%, 45 min) and phenol (96%, 75 min) than that of BCN (RhB: 20%, 45 min; phenol: 30%, 75 min) (Figure 7c,d).

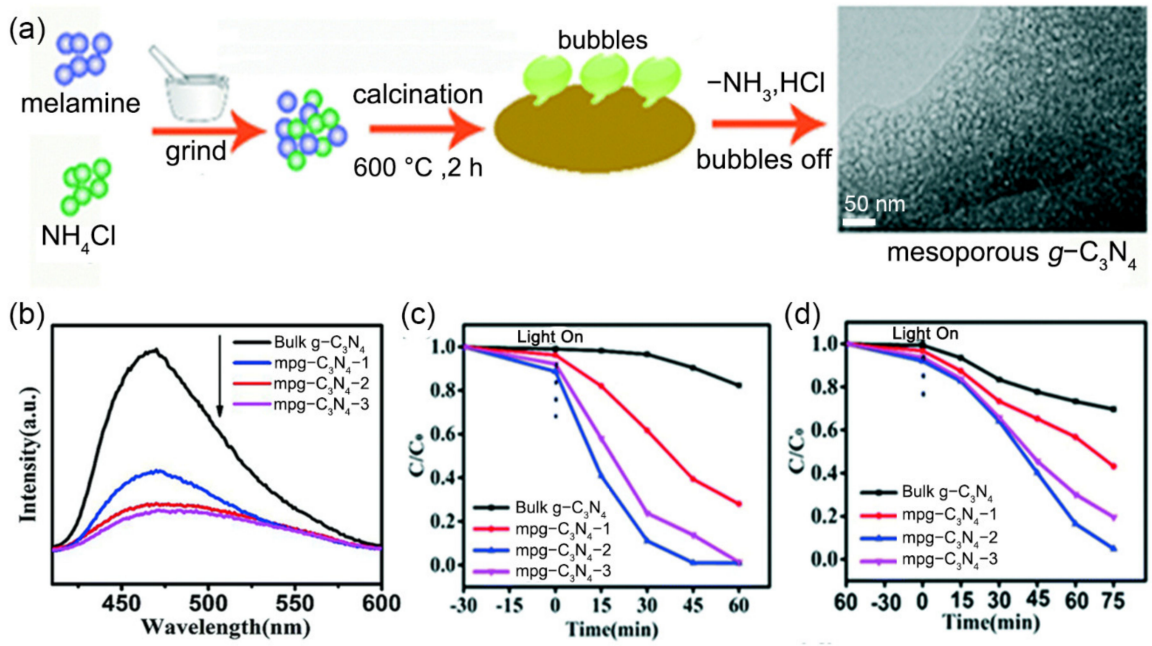

Figure 7. (**a**) Synthesis process of mesoporous *g*-C_3N_4; (**b**) PL spectra of the BCN and mesoporous mp*g*-C_3N_4 photocatalysts; visible light photodegradation rate constants of (**c**) RhB and (**d**) phenol of mp*g*-C_3N_4. Reprinted with permission from [126] 2011 Royal Society of Chemistry.

Except for gas release to modify the pore structure, decomposition co-products of soft templates could couple with *g*-C_3N_4 to create charge transfer interfaces. For instance, Chen et al., utilized $SnCl_4$ as a pore modifier and thiourea as precursor, obtaining macroporous *g*-C_3N_4/SnO_2 nanohybrids (Figure 8a) [127]. During the synthesis process, $SnCl_4$

was hydrolyzed to hydrous SnO_2 and HCl. SnO_2 was coupled with g-C_3N_4 to yield g-C_3N_4/SnO_2 hybrids. At the same time, the released gaseous HCl acted both as an erosive soft template to tune the pore formation, giving the hybrids a pore size of 100–430 nm, a higher SSA of 44.3 $m^2 \cdot g^{-1}$ (6.5 times of BCN), and a higher pore volume of 2.638 $cm^3 \cdot g^{-1}$ (only 0.875 $cm^3 \cdot g^{-1}$ for BCN). As the continuous macropore channels favored light penetration into the solid samples and the larger volume of moderate macropores led to deeper optical penetration, the light absorption range was extended to 800 nm. Furthermore, because of the larger contacted area between g-C_3N_4 and SnO_2, efficient photoinduced electron transfer across the interface was observed, as suggested by ~90% PL quenching (Figure 8b) and remarkably enhanced photocurrent generation (Figure 8c). As the result of macropore structure and the heterojunction, the MB degradation rate of macropores g-C_3N_4/SnO_2 nanohybrid reached 98% in 100 min, which was 2.4 times higher than that of BCN (Figure 8d).

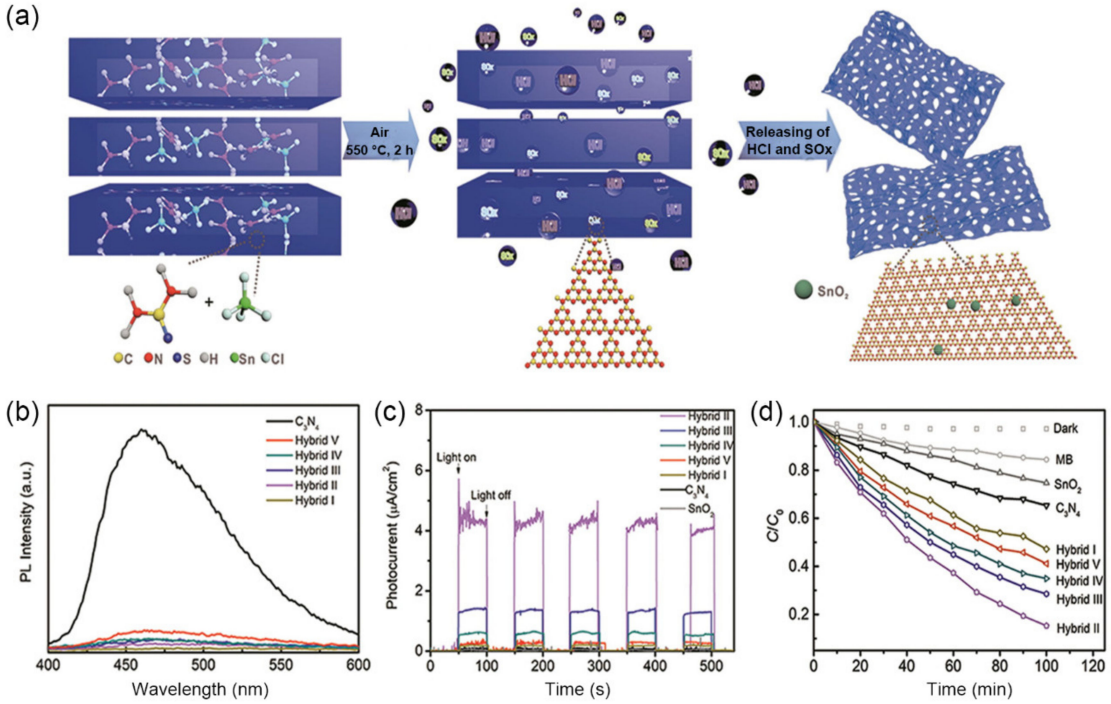

Figure 8. (**a**) Synthesis process of highly macroporous g-C_3N_4 system; (**b**) PL emission spectra and (**c**) photocurrent plots of the hybrids; (**d**) photocatalytic degradation of MB of the hybrids using under solar light, Reprinted with permission from [127] 2019 Elsevier.

3.2.3. g-C_3N_4 Precursors as Templates

Copolymerization is one of the most common synthetic approaches to preparing CN materials with extended light absorption [128–131]. In this technique, a mixture of two or more small organic monomers, obtained by grinding, ball-milling, or dissolution in common solvents, reacts at a high temperature, yielding CN materials [132]. Inspired by copolymerization, the choice of soft template is gradually shifting to the precursor itself without introducing other elements. The research about using two kinds of precursors to prepare the porous g-C_3N_4 increases gradually. One of the precursors is used as the template to form the pore structure, while the other acts as the main precursor of g-C_3N_4 matrix.

As the direct polymerization of urea can produce porous g-C_3N_4 without tailoring the reaction pressure and atmosphere, urea usually serves as a natural pore-forming agent [133]. For instance, porous g-C_3N_4 with a surface area of 60 $m^2 \cdot g^{-1}$ has been produced on a large scale by pyrolysis of urea and DCDA in air [134]. The rate content of optimum porous g-C_3N_4 for phenol decomposition was 0.039 h^{-1}, which was 2.8 times as high as BCN. In another work, melamine was pre-treated in thiourea solution, and then

the modified precursor samples were calcined to obtain porous, thin *g*-C_3N_4 nanosheets whose SSA increased from 9.0 to 44.2 $m^2 \cdot g^{-1}$ [135]. A 3.3-fold higher photocatalytic performance for H_2 evolution (99.1 $\mu mol \cdot h^{-1}$) was achieved, in comparison with pristine one (29.7 $\mu mol \cdot h^{-1}$). Thiourea has the similar feature as urea, and was consequently used as a soft template. For example, thiourea was decomposed into gas bubbles during calcination, thereby inducing pore structure when copolymerized with DCDA [136]. This porous *g*-C_3N_4 with an average pore size of 3.7 nm, resulted in a 3.4-fold enhancement of SSA (46.4 $m^2 \cdot g^{-1}$) and an enhanced photocatalytic rate in the photodegradation of MB (0.146 h^{-1}) with respect to the BCN (0.0430 h^{-1}).

Besides forming pores by generating gas bubbles, heating-induced shrinking of the precursor framework can also help with the pore structure. Taking melamine sponge as soft template and urea as precursors, macroscopic 3D porous *g*-C_3N_4 monolith (PCNM) was synthesized with a pore diameter of 200–400 nm, SSA of 78 $m^2 \cdot g^{-1}$, and pore volume 0.76 $cm^3 \cdot g^{-1}$ [30]. Illustration of the preparation of a macroscopic 3D PCNM as shown in Figure 9a. Owing to the multiple reflections of incident light within the interconnected network of porous *g*-CN nanosheets, PCNM showed significantly improved light-harvesting ability above 450 nm in the optical spectrum compared to the powdered *g*-CN (Figure 9b). Furthermore, the 3D interconnected network of porous nanosheets ensured sufficient mass transportation. It shortened the diffusion length of charge migration, thus facilitating electron re-localization on surface edge sites to hinder the charge recombination, which could be suggested as a much smaller arc radius in EIS results (Figure 9c) and 2.5-fold increased photocurrent density (inset in Figure 9c). The prepared mesoporous *g*-C_3N_4 had a rate of H_2 evolution of 29.0 $\mu mol \cdot h^{-1}$, which was 2.84 times that of ordinary *g*-C_3N_4 powder (Figure 9d).

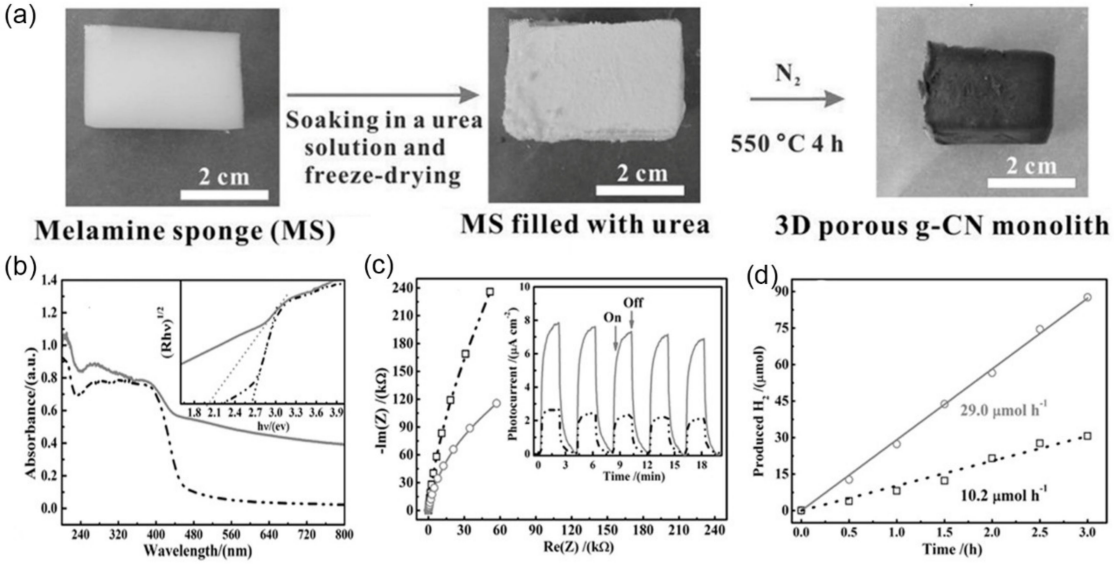

Figure 9. (**a**) Synthesis process of macroscopic 3D PCNM; (**b**) photocatalytic activity of H_2 evolution; (**c**) EIS plots (inset: photocurrent-time dependence); and (**d**) DRS spectrum of PCNM (solid line) and the *g*-C_3N_4 powder (dotted line), Reprinted with permission from [30] 2015 John Wiley and Sons.

There are several advantages of soft-template method. Firstly, the selection of soft templates is very rich and diverse. It makes the adjustment of sample structure more flexible, and the morphology of the pore structure can be adjusted by modifying the experimental design and preparation conditions. Secondly, the soft-template method can simplify the experimental process by reducing the removing step. Thereby, toxic and harmful reagents are avoided in the preparation process, which has less harm to the environment. Thirdly, the resulting lamellar and channel structures are conducive to light capture, improving light utilization and producing more photogenerated carriers. The disadvantage of

the soft-template method is that it cannot always strictly control the size and morphology of the pores, so that prepared samples are not as orderly as the hard-template method. There are phenomena of interlayer collapse, interlayer stacking, and molecular polymerization, which hinder electron transmission. In addition, some soft templates have self-assembly behavior, which makes the reaction insufficient and leads to the failure of reaching the ideal SSA. Furthermore, some by-products will remain on the structure, cover the active sites, and affect the catalytic efficiency. Therefore, developing a green synthesis route to obtain PCN with high performances by soft-template methods remains challenging.

3.3. Template-Free Method

Template-free method refers to the construction process of pore structure by only one kind of precursor without involving a second template. According to literature research, there are mainly two ways to achieve template-free modification of pore structure: pre-treatment and a top-down approach. Pre-etching means that the pore of *g*-C_3N_4 is formed by condensation of hydro- or acid-treating precursors. Recently, thermal condensation of supramolecular precursors has emerged as a physiochemical approach to form the pore structure of *g*-C_3N_4, and the top-down approach is an exfoliation technique, especially for the synthesizing of porous *g*-C_3N_4 sheets from BCN. The template-free method could eliminate the step of template preparation, simplify the experimental process from sample preparation to the greatest extent, and reduce the cost at the same time.

3.3.1. Pre-Etching of *g*-C_3N_4 Precursors

Porous *g*-C_3N_4 can be obtained via direct thermal calcination of the pre-treated precursors [137–139]. Hydrothermal pre-treatment is the most simple, economical, and convenient way, by which the pore structure could be formed without changing the crystal structure or chemical structure of precursors. For instance, porous *g*-C_3N_4 was produced through hydrothermal-treated cyanamide's thermal polymerization [138]. Specifically, cyanamide solution was first heated at 150 °C, and then as-prepared white precursor was heated at 550 °C for polymerization. Many uniform pores (~30 nm) on *g*-C_3N_4 surface were driven by the etching effect of ammonia gas released during the hydrothermal pre-treatment process. The as-prepared porous *g*-C_3N_4 possessed an increased SSA (18.1 $m^2 \cdot g^{-1}$) in comparison to BCN (6.6 $m^2 \cdot g^{-1}$), and 7.2-fold higher photocatalytic H_2 evolution rates (958 $\mu mol \cdot h^{-1} \cdot g^{-1}$) than that of BCN.

A bottom-up acidification strategy refers to direct calcination of pre-formed precursor by hydrothermal treating in diluted acid solution. Previously reported works suggested that the acid, such as HCl, H_2SO_4 [140,141], H_3PO_3 [142], would act as an etching agent for nitrogen-rich precursor molecules, which contribute to the formation of pores during the polymerization of the acidified precursors. For example, *g*-C_3N_4 with a thin, porous platelet-like structure (p-*g*-C_3N_4) was fabricated via the polymerization of HCl-acidified melamine [143]. The *g*-C_3N_4 derived from HCl-acidified melamine exhibited a larger SSA (69.0 $m^2 \cdot g^{-1}$) than that of *g*-C_3N_4 derived from pure melamine (17 $m^2 \cdot g^{-1}$). The degradation constants of p-*g*-C_3N_4 were calculated to be 0.131 min^{-1}, which was 9.4 times higher than *g*-C_3N_4. Similarly, Zhang et al., first treated the precursor melamine with HCl and alcohol and used it to prepare *g*-C_3N_4 photocatalyst (a*g*-C_3N_4) with a mesopore structure (pore size: 30.3 nm) (Figure 10a,b) [144]. The SSA and pore volume of a*g*-C_3N_4 (26.2 $m^2 \cdot g^{-1}$; 0.121 $cm^3 \cdot g^{-1}$) was higher than that of *g*-C_3N_4 (12.7 $m^2 \cdot g^{-1}$; 0.049 $cm^3 \cdot g^{-1}$), respectively. More active sites provided by a higher SSA facilitate the increase in active species for photocatalytic reaction, as proven by the increased fraction of the shorter-range charge carriers of a*g*-C_3N_4 (50.52%) for *g*-C_3N_4 (53.88%) (Figure 10c). In the presence of a*g*-C_3N_4, the RhB degradation efficiency rate was 99.9%, while with the catalysis by *g*-C_3N_4, the RhB degradation efficiency was only 62.6% (Figure 10d).

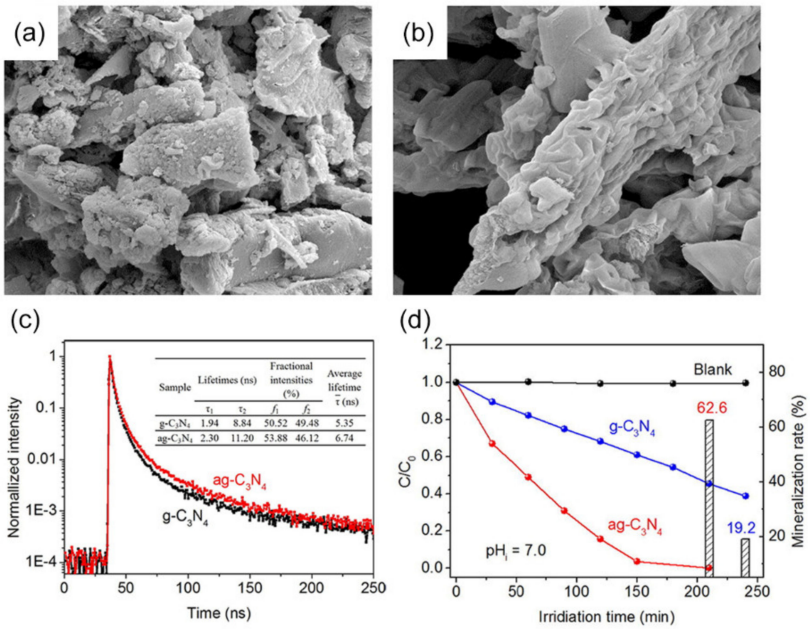

Figure 10. SEM images of (**a**) pristine *g*-C_3N_4 and (**b**) a*g*-C_3N_4; (**c**) time-resolved fluorescence decay spectra, and (inset) two-exponential analysis results of *g*-C_3N_4 and a*g*-C_3N_4; (**d**) comparison of PCD efficiency and mineralization rate of RhB by *g*-C_3N_4 and a*g*-C_3N_4 [144]. Reprinted with permission from [144] 2014 Elsevier.

3.3.2. Supramolecular Precursors

Recently, tuning porosity in CN through alteration supramolecular precursors has emerged entirely to be a new physiochemical approach [145]. In this approach, precursor monomers interact by non-covalent interactions (hydrogen bonding, π-π stacking, electrostatic interactions, etc.), forming a versatile self-assembled supramolecular in a given solvent. Designing the arrangement of the precursor monomers prior to the calcination leads to good control of the final *g*-C_3N_4 morphology and porosity, photophysical, and catalytic properties.

From a strengthened perspective, hydrogen bonds were mainly used to manipulate the monomer sequence designs, due to their exceptional strength and abundant donor and acceptor sites. A typical example is cyanuric acid-melamine supramolecular. It has been reported that cyanuric acid would be capsulated by melamine through hydrogen-bonding interaction and prohibit the polymerization of melamine to a certain extent. In one work, a porous *g*-C_3N_4 (p-CN) with a 3D hierarchical framework was obtained by thermal condensation of cyanuric acid-melamine supramolecular, featuring a 3.6-times larger SSA (35.6 $m^2 \cdot g^{-1}$) than that of BCN [146]. Besides, the hierarchical porous structure improved light-harvesting capacity and provided more active sites for photocatalytic reactions. As a result, p-CN showed an increased H_2 evolution rate (68.5 $\mu mol \cdot h^{-1}$), which was approximately 4.8 times than that of BCN (14.3 $\mu mol \cdot h^{-1}$). In addition to the widespread utilization of the cyanuric acid-melamine supramolecular, the diversity of supramolecular structures formed by the self-assembly of the precursors has been reported to modify the final CN properties for an enhanced photoactivity, such as cyanuric acid-melamine-urea [147], melamine-urea [148], and dicyandiamide-urea [149].

Solvents used in the aggregation of supramolecular assemblies are key for the pore structure of *g*-C_3N_4. Solvents can serve as building blocks in the formation of supramolecular assemblies due to their hydrogen bonding sites. As an example, Zhu et al., obtained ultrathin *g*-C_3N_4 nanosheets (*g*-CN(*x*), *x* = 0.5, 1.0, 2.0 presented the concentration of HNO_3) by calcining the HNO_3-treated melamine supramolecular complexes (Figure 11a) [150]. The melamine supramolecular complexes were prepared by putting melamine in 1.0 $mol \cdot L^{-1}$ nitric acid, during which the NH . . . O (N) hydrogen-bonded supramolecular complexes

formed through the interaction between melamine and HNO_3. The broken hydrogen bond made *g*-CN(1.0) samples possess mesoporous/macroporous structures with a pore diameter of 10–100 nm. Besides, the SSA of *g*-CN(1.0) was 59.2 $cm^2 \cdot g^{-1}$, which was higher than bulk *g*-CN (15.6 $cm^2 \cdot g^{-1}$). Additionally, optimized ultrathin nanosheets with a porous structure are favorable for a photogenerated carrier effective transfer and separation, as suggested by a smaller arc radius of *g*-CN(1.0) on the EIS plots (Figure 11b), compared with BCN. As a result, the RhB degradation efficiency of *g*-CN(1.0) (0.352 min^{-1}) was almost 10 times higher than that of the BCN (Figure 11c). Inspired by traditional liquid-liquid interfacial polymerization [151], interfacial supramolecular organization on two non-miscible solvents emerged in the modification of CN structure [152,153]. The choice of solvents plays an important role in the formation of supramolecular assembly at the interface of the solvents. For example, Dolai et al., employed water/chloroform interface to pre-organize precursor monomers (cyanuric acid and melamine), and added picric acid to tailor supramolecular framework structure so as to obtain the final CN porosity [154]. As the content of picric acid was increased, the tube-like structure of *g*-C_3N_4 gradually became more perforated, giving a sponge-like structures. An impressive enhancement of the SSA was obtained from 54 to 106 $m^2 \cdot g^{-1}$.

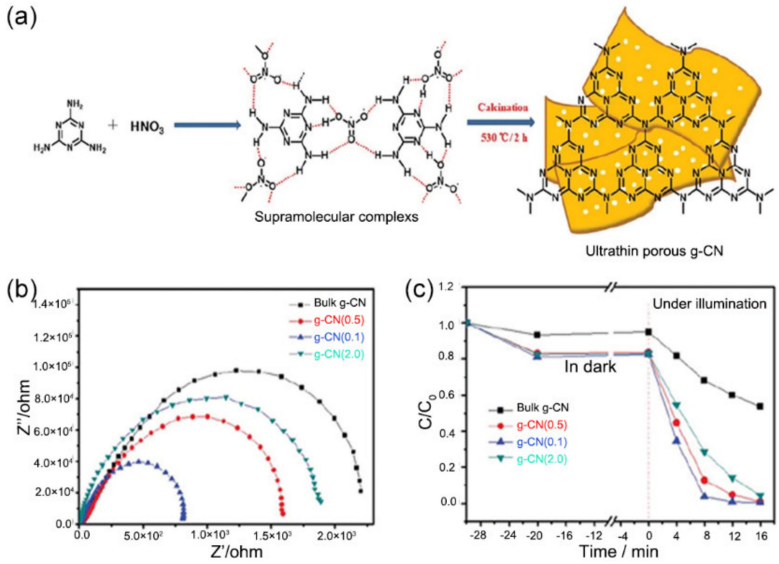

Figure 11. (**a**) Synthesis process of ultrathin porous *g*-CN nanosheets; (**b**) EIS Nyquist plots; and (**c**) photocatalytic RhB degradation rate constant of *g*-CN(x) and BCN, Reprinted with permission from [150]. 2019 Springer Nature.

Recently, the utilization of highly ordered supramolecular single crystals based on CN monomers has been exploited as an effective approach to control the properties of CN materials [155,156]. Barrio et al., synthesized melaminium chloride hemihydrate single crystals, where protonated melaminium were connected by Cl^- and H_2O [157]. By using such supramolecular single crystals as a precursor, the obtained needle-like porous CN nanostructure had an SSA of 185 $m^2 \cdot g^{-1}$, and an increased visible light absorption capacity in range of 450–600 nm. Besides, triazine-based cocrystals composed of two types of molecular units by non-covalent interactions, such as acetoguana-mine-melamine [158] and terephthalic acid-melamine [159], were selected as precursors for porous CN via pyrolysis. MOFs have emerged as a new type of precursors for porous carbons-based material and metal/carbon composites [160,161]. Due to the highly ordered crystalline structures, MOFs would be good candidates for use as sacrificial templates and precursors to give porous *g*-C_3N_4 [162]. Moreover, metal nodes transformed to metallic oxide under proper thermal condensation conditions, which would be further enhanced by forming heterojunction with *g*-C_3N_4. In one case, Wang et al., prepared porous nanorod-like *g*-C_3N_4/CuO composites by using a copper-melamine supramolecular framework as a precursor [163]. The nanorods

had a pore size of about 20–50 nm, with the SSA of 15.37 $m^2 \cdot g^{-1}$, which was about three times higher than pure *g*-C_3N_4 (5.26 $m^2 \cdot g^{-1}$). Almost 94% of the RhB was degraded by *g*-C_3N_4/CuO under 20 min visible-light irradiation, while only 12% and 5% of RhB was degraded by *g*-C_3N_4 and CuO, respectively.

3.3.3. Top-Down Approach

Because of the weak van der Waals force between layers in BCN frameworks, 2D porous *g*-C_3N_4 nanosheets were usually prepared by exfoliation from BCN. Such a pore-forming method was called the top-down approach. Recently, liquid exfoliation [164] or thermal exfoliation [165] strategies have also been employed to yield porous *g*-C_3N_4 nanosheets.

There are two main liquid exfoliation techniques for preparing porous *g*-C_3N_4 nanosheets: ion intercalation and ultrasound assist [166]. In one work, porous *g*-C_3N_4 nanosheets were obtained by lithium chloride ions in situ intercalating bulk materials in the thermal polycondensation process and followed by liquid exfoliation in water [167]. The nanosheets with 2–3 nm thickness and high-density in-plane pores with 2–3 nm gave a higher SSA of 186.3 $m^2 \cdot g^{-1}$ compared to BCN (9.8 $m^2 \cdot g^{-1}$). An enhanced H_2 evolution performance for nanosheets (107.84 $\mu mol \cdot h^{-1}$) was observed, which was more than six times higher than that of bulk one (16.31 $\mu mol \cdot h^{-1}$). A more recent strategy for liquid exfoliation is to expose the BCN to ultrasonic waves in a solvent. Mesoporous *g*-C_3N_4 nanosheets (CNS) were fabricated by ultrasonically exfoliating the BCN [168]. SEM images are shown in Figure 12a. The as-prepared *g*-C_3N_4 nanosheets presented a higher SSA (55.41 $m^2 \cdot g^{-1}$) and a larger mesoporous volume (0.216 $cm^3 \cdot g^{-1}$) in comparison with the bulk counterpart (SSA: 7.61 $m^2 \cdot g^{-1}$; pore volume: 0.055 $cm^3 \cdot g^{-1}$). The resulting narrow bandgap (2.51 eV) (Figure 12b), wide light response (250–800 nm) (Figure 12c), and lower charge transfer resistance (Figure 12d) all contributed to a 3.3-fold photocatalytic H_2 evolution rate of mesoporous *g*-C_3N_4 (97.6 $\mu mol \cdot g^{-1} \cdot h^{-1}$), compared to that of the BCN (29.8 $\mu mol \cdot g^{-1} \cdot h^{-1}$).

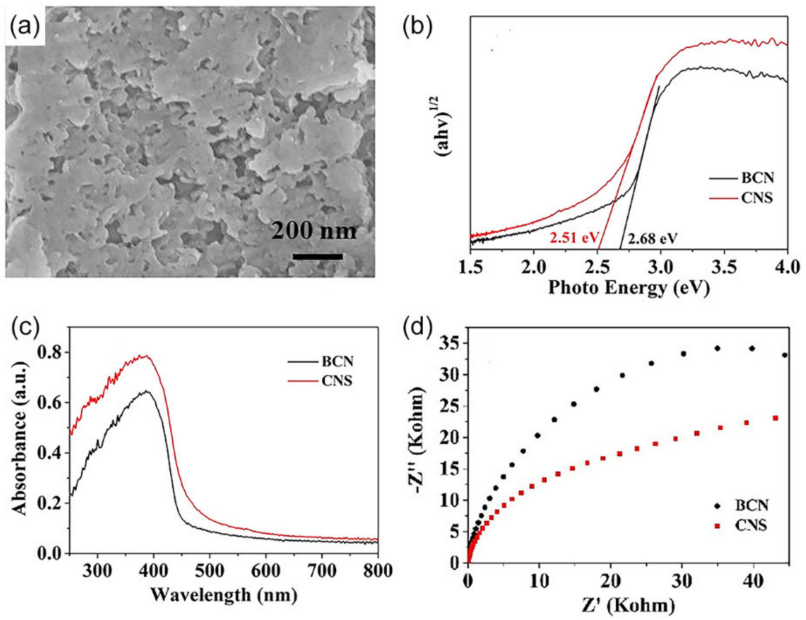

Figure 12. (**a**) SEM image of CNS; (**b**) estimated bandgaps, (**c**) UV-vis DRS, and (**d**) EIS plots of the BCN and CNS, Reprinted with permission from [168] 2021 Elsevier.

It has been found that BCN can initially be thermally oxidized into nanosheets by overcoming the weak van der Waals force between layers [169]. Moreover, during the heating process, some tri-s-triazine units consisting of C-N bonds could also be "etched", giving rise to the pore of *g*-C_3N_4 [170]. By increasing the calcination time, *g*-C_3N_4 with various pore sizes could be obtained by further thermal oxidation. Li and coworkers fabricated holey

ultrathin g-C_3N_4 nanosheets (CNHS) (thickness: 9.2 nm) with abundant micro- (1–2 nm), meso- (2–50 nm), and macropores (50–100 nm) by thermal exfoliation of bulk g-C_3N_4 (CNB) at 520 °C for a continuous 6 h (Figure 13a) [75]. The SSA of CNHS was 277.98 $m^2 \cdot g^{-1}$, almost 26 times higher than that of CNB (10.89 $m^2 \cdot g^{-1}$). Compared to CNB, the CB potential of CNHS upshifted about 0.25 V (Figure 13b), which might lead to a larger thermodynamic driving force in photocatalytic hydrogen production. This larger bandgap could ascribe to the quantum confinement effect and the existence of in-plane holes, which decreased the conjugation system of g-C_3N_4. Moreover, the large number of in-plane holes greatly facilitated the mass transfer and improved photogenerated charge mobility, as suggested by smaller charge transfer resistance (Figure 13c) and higher photocurrent response (inset in Figure 13c) CNHS. Given the above, CNHS exhibited 22.24 times higher H_2 evolution rate of 57.20 $\mu mol \cdot h^{-1}$, than that of CNB (2.57 $\mu mol \cdot h^{-1}$) (Figure 13d).

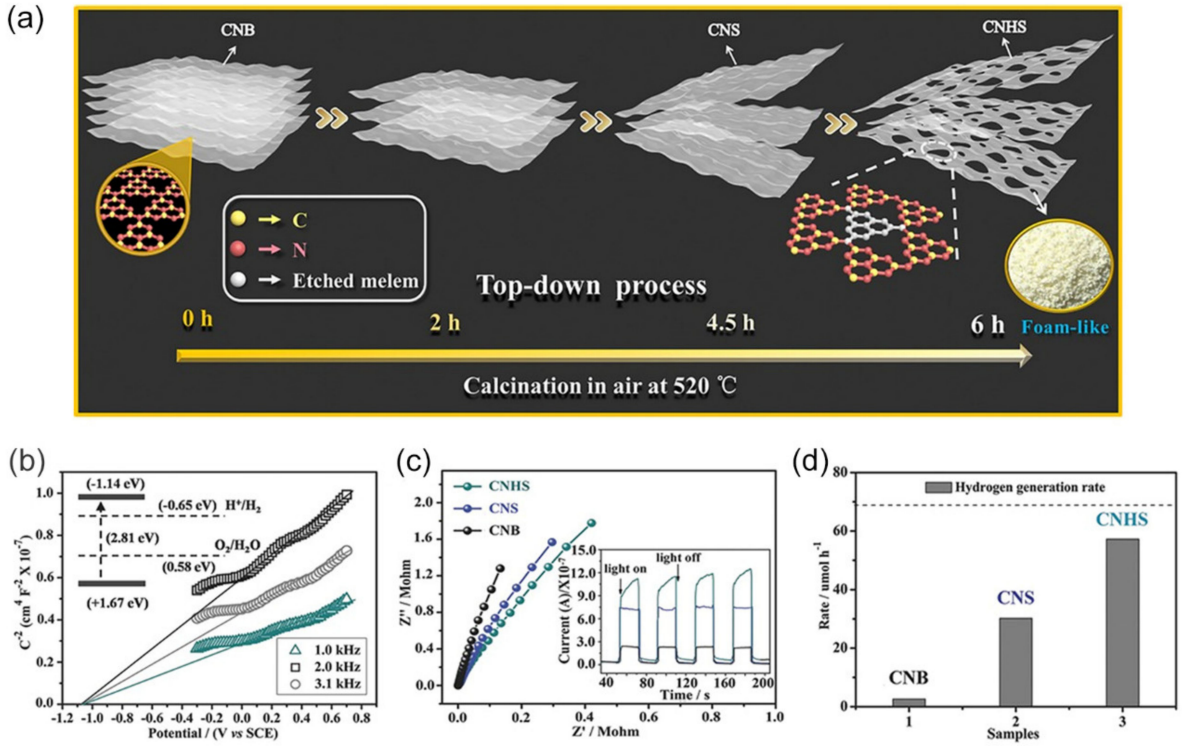

Figure 13. (**a**) Synthesis process of foam-like CNHS by top-down strategy; (**b**) Mott–Schottky plots with various frequencies of CNHS; (**c**) EIS plots (inset: transient photocurrent response) and (**d**) photocatalytic H_2 evolution rate of CNB and CNHS, Reprinted with permission from [75] 2016 John Wiley and Sons.

The advantage of the template-free method is that it can produce the pore structure by pre-treating precursors or exfoliating BCN. This can greatly reduce the consumption of raw materials and avoid using toxic and harmful reagents. Besides, there is no template residue in the preparation process, thus avoiding the negative impact caused by the existence of the template to the greatest extent. The biggest disadvantage of the template-free method is that its porous structure is formed by a natural reaction, so it is difficult to regulate the pore volume, pore diameter, and SSA of the samples. Secondly, due to the lack of template participation, g-C_3N_4 lacks effective support. Consequently, the phenomenon of molecular aggregation and interlayer stacking of samples prepared by a template-free method is common, resulting in unsatisfactory SSA.

Achievements of previous studies on pore modification of g-C_3N_4 have been concluded in Table 1. As discussed earlier, the pore modification method results in different structure regularity and SSA of the samples, arranged as follows: hard-template method > soft-template method > template-free method. This result is mainly because the different

pore-support abilities of templates. The hard-template method requires a template removal step, which is inevitable and may use toxic and harmful reagents, so the hard-template method is gradually transitioning to the soft-template method or template-free method. However, the soft-template method has the problem of template residue covering the active site, which reduces catalytic efficiency. The pore structure formed by the template-free method is not easy to adjust and control, and interlayer stacking makes the SSA less than ideal. Therefore, specific strategies towards each pore structure modification have been studied. In the above cases, the sample prepared by the hard-template method has a higher SSA, but it increases the probability of recombination of electron holes. Therefore, energy band regulation is needed: different energy levels of other substances are used to form potential differences with the energy levels of *g*-C_3N_4 itself to promote electron transfer, thus greatly inhibiting the recombination of electrons and holes. The template support of the soft-template method is weak, the SSA of samples obtained by this method is smaller than that of a hard-template method, so that there are fewer active sites. Therefore, the precursors and soft templates should be reasonably selected. The special 3D structure should be combined to enhance the capture of light, to improve the utilization of light, and increase the number of photogenerated carriers. Template-free method used no template support during the process. The pore structure is mainly from chemical reaction and bubble escape, which leads to the difficulty to control the structure, prone to interlayer collapse and other phenomena, covering the active site. Therefore, it is necessary to use element doping to improve the electron transmission rate and increase the photoelectric current. The modification means that the three preparation methods are interrelated, and the effect is different, which should be selected according to the morphology and photoelectric properties of the sample.

Table 1. Summary of the different template methods in adjusting the pore structure of *g*-C_3N_4 and their photocatalytic performance.

Sample	Template	Removal Reagents	Pore Size (nm)	Pore Volume ($cm^3 \cdot g^{-1}$)	SSA ($m^2 \cdot g^{-1}$)	Photocatalytic Application (Efficiency)	References
Hard-template method							
Meso-*g*-C_3N_4/WP/Meso-*g*-C_3N_4	SiO_2	HF	12	-	82	H_2 evolution (198.1 $\mu mol \cdot h^{-1} \cdot g^{-1}$)	[171]
Porous-C_3N_4	SiO_2	HF	5–40	-	209	MB degradation (85% in 180 min)	[85]
mp*g*-$C_3N_{4-\delta}$	SiO_2	NH_4HF_2	12.54	0.69	218.15	RhB degradation (30.2% in 30 min)	[172]
mesoporous *g*-C3N4	SiO_2	NH_4HF_2	12	0.52	190.7	U(VI) reduction (73% in 60 min)	[87]
TiO_2 trapped *g*-C_3N_4	PSB	NH_4HF_2	27	0.30	37	RhB degradation (100% in 50 min)	[173]
CN-MCF-0.4	MCF	NH_4HF_2	5.3	1.36	498	Knoevenagel condensation (93.6% in 240 min)	[174]
C_3N_4-MCF	MCF	HF	5/20	0.30	70	CO_2 reduction (8.0 $\mu mol \cdot g^1$)	[94]
g-C_3N_4(GLBM-SBA-15)	SBA-15	NH_4HF_2	11/90	0.43	145	MO degradation (90% in 30 min)	[83]
macrostructure *g*-C_3N_4	NaCl	H_2O	-	-	16.71	H_2 evolution (459 $\mu mol \cdot h^1 \cdot g^{-1}$)	[109]
Na^+ functionalized porous *g*-C_3N_4 nanorods	$Na_2S_2O_3$	H_2O	4.25	-	29.72	H_2 evolution (9796 $\mu mol \cdot h^1 \cdot g^{-1}$)	[103]
Na_2CO_3-embedded porous crystalline *g*-C_3N_4	$NaHCO_3$	H_2O	3/30	0.09	15.34	H_2 evolution (1010 $\mu mol \cdot h^1 \cdot g^1$)	[175]
polymeric CN nanocages	ZnO	HCl and $NH_3 \cdot H_2O$	16.8	0.103	32	H_2 evolution (227.23 $\mu mol \cdot h^1 \cdot g^{-1}$)	[176]
Soft-template method							
g-C_3N_4	P123	-	20	-	90	H_2 evolution (60.6 $\mu mol \cdot h^1$)	[123]
3D mesoporous CN	ionic liquid	-	15	0.85	381	H_2 evolution (129.5 $\mu mol \cdot h^{-1}$)	[177]
hollow mesoporous *g*-C_3N_4 sphere	ionic liquid	-	9.7	-	84	H_2 evolution (157 $\mu mol \cdot h^{-1}$)	[28]
g-C_3N_4/SnO_2	HCl, H_2O	-	100/430	2.638	44.3	MB degradation (72% in 100 min)	[127]
porous *g*-C_3N_4 nanosheets	NH_3, CO_2	-	5/70	-	92.75	H_2 evolution (1437 $\mu mol \cdot h^1 \cdot g^{-1}$)	[178]
Macroscopic 3D porous *g*-C_3N_4 monolith	melamine	-	4/30–170	0.76	78	H_2 evolution (29 $\mu mol \cdot h^{-1}$)	[30]

Table 1. *Cont.*

Sample	Template	Removal Reagents	Pore Size (nm)	Pore Volume ($cm^3 \cdot g^{-1}$)	SSA ($m^2 \cdot g^{-1}$)	Photocatalytic Application (Efficiency)	References
Template-free method							
Thin-layered *g*-C_3N_4 nanosheets	-	-	4/20–100	0.752	92.8	H_2 evolution (1391 $mmol \cdot h^1 \cdot g^{-1}$)	[86]
g-C_3N_4/TiO_2	-	-	11	0.193	70.2	RhB degradation (0.0478 min^{-1})	[80]
S-doped CN	-	-	17.04	0.464	108.9	H_2 evolution (567.7 $\mu mol \cdot h^1 \cdot g^{-1}$)	[179]
oxygen-doped *g*-C_3N_4 nanosheets	-	-	5–100	-	-	H_2 evolution (189.3 $\mu mol \cdot h^{-1}$)	[180]
Porous *g*-C_3N_4 nanosheets	-	-	5–25	0.61	190.1	MB degradation (44.7% in 30 min)	[181]
mp*g*-C_3N_4/rGO	-	-	10–80	0.419	85	RhB degradation (99.7% in 40 min)	[61]
porous *g*-C_3N_4	-	-	4.5/40.5	0.211	44.2	H_2 evolution (99.1 $\mu mol \cdot h^{-1}$)	[135]

4. Application

g-C_3N_4 possesses a moderate bandgap of 2.7 eV, with the CB and VB positions respectively at −1.4 eV and 1.3 eV (vs. NHE). Such band structure enables *g*-C_3N_4 to generate the active free radicals, photogenerated electrons, and holes with strong oxidization and reducibility for various photocatalytic applications. In coping with energy crises, *g*-C_3N_4 can split water into H_2 and O_2 and reduce CO_2 into energy rich compounds. For environmental remediation, it can degrade several organic and inorganic pollutants into harmless substances. As discussed earlier, the photocatalytic efficiency of porous *g*-C_3N_4 has been improved compared with pristine *g*-C_3N_4. Based on tuning the pore structure of *g*-C_3N_4, researchers have carried out various modification strategies for enhancing photocatalytic efficiency to reach the desired effect, such as structure optimization, vacancies modify, element dope, and heterostructure construct. In view of this, the research progress of modified porous *g*-C_3N_4 in the field of different photocatalytic application are discussed in the following section.

4.1. Water Splitting

Photocatalytic water splitting to produce H_2 and O_2 is an attractive approach for the development of clean and renewable energy development. To realize water splitting, the CB of semiconductor photocatalysts must be more negative than the reduction potential of H+/H_2 (0 V vs. NHE), and VB must be more positive than the oxidation potential of H_2O/O_2 (1.23 V vs. NHE). The position CB and VB of *g*-C_3N_4 at −1.4 and 1.3 eV, respectively, are highly suitable for carrying out the given redox reaction abilities. Besides, *g*-C_3N_4 with the bandgap of 2.7 eV exceed the free energy (1.23 eV) of water splitting under light irradiation. The excited electrons can cause the H^+ reduction reaction to evolute H_2, while the holes can cause OH^- oxidation reaction to form O_2. Thus, *g*-C_3N_4 has the ability of overall water splitting to obtain H_2 and O_2. Significant achievements have been obtained on the porous *g*-C_3N_4 based photocatalysts for water splitting activity.

Several typical nanostructures of porous *g*-C_3N_4 have been applied in water splitting, such as one-dimensional (1D) nanotubes [182–184], 2D nanosheets [185–188], 3D hierarchical porous structure [141,189–192]. 1D nanostructures are usually arranged in an orderly long range, thus leading to low surface defect density and increased carrier mobility. By using melamine-oxalic acid supramolecules as soft template, porous *g*-C_3N_4 nanotubes (length: 200–400 nm; diameter: 100–200 nm) were obtained, labeled as *g*-C_3N_4(NT) [193]. *g*-C_3N_4(NT) had the average pore diameters of 26.8 nm and the increased SSA of 122.5 $m^2 \cdot g^{-1}$ compared to BCN (10.3 $m^2 \cdot g^{-1}$). Due to the stabilized electron migration along a preferential direction, the decay lifetime of *g*-C_3N_4(NT) was prolonged to 27.4 ns from 5.25 ns of BCN, indicating the decreased recombination photoexcited electrons and holes. The H_2 evolution rate of *g*-C_3N_4(NT) was 214.5 $\mu mol \cdot h^{-1}$, which was about 12-fold higher than BCN (16.8 $\mu mol \cdot h^{-1}$). Fabrication of 2D nanostructures could not only provide a large SSA, but

also enable rapid transfer of photogenerated charge carriers onto the surface of photocatalysts, promoting charge separation [194]. In one case, porous, thin *g*-C_3N_4 nanosheets (CN*x*, *x* = 0, 1, 2, 3 presented molar ratios of melamine to thiourea of 1:0, 1:1, 1:3, and 1:6) were obtained by a template-free method which used thiourea-assisted hydrothermal pre-treated melamine as precursor [136]. During the hydrothermal process, thiourea decomposed into H_2S and NH_3, resulting in the surface etching and deep peeling of melamine. Thus, after calcination, the porous *g*-C_3N_4 nanosheets CN1 not only exhibited the increased SSA (from 9.0 to 44.2 $m^2 \cdot g^{-1}$), but also showed the promoted charge separation (Figure 14a). As proved by the photocurrent response, CN1 had the stronger photocurrent density, which could be up to approximately three times that of BCN (Figure 14b). Therefore, the CN1 showed 3.3-fold increased photocatalytic performance for H_2 evolution (99.1 $\mu mol \cdot h^{-1}$), in comparison with BCN (29.7 $\mu mol \cdot h^{-1}$) (Figure 14c). It should be noted that the ratio between the two precursors affects the pore structure. As in this case, when the thiourea is present in excess, large volumes of gas, this would cause the collapse of the pore structure, which could explain the lower H_2 evolution rate of CN3 than BCN.

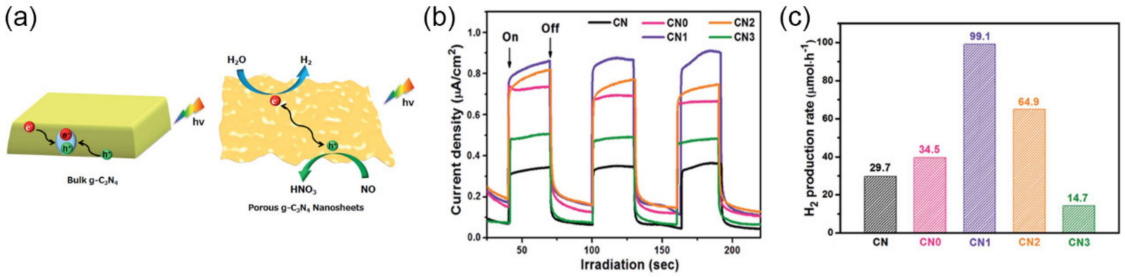

Figure 14. (**a**) Diagram for charge separation of BCN and porous *g*-C_3N_4 nanosheets; (**b**) transient photocurrent responses and (**c**) photocatalytic H_2 evolution rate constants of all samples under visible light (λ > 420 nm), Reprinted with permission from [135] 2012 Royal Society of Chemistry.

It has been demonstrated that controlling the concentration and distribution of surface vacancy could effectively expand the light response range, tune the energy band structure, and provide more active centers. As shown in one research paper, the carbon vacancies gave porous *g*-C_3N_4 a broad light absorption band which even extended into the near-infrared region (800–1400 nm) [195]. Heat treatment of *g*-C_3N_4 in the reduced atmosphere, such as H_2 [196] and NH_3 [197], can lead to the release of surface atoms and consequently the simultaneous production of homogeneous vacancies on the surface of *g*-C_3N_4. For instance, Tu et al., prepared porous *g*-C_3N_4 nanosheets with nitrogen vacancies (C/N = 0.66) by heating the BCN to 525 °C in H_2 atmosphere, named CN-525 [198]. The pores with an average diameter of about 20 nm could be observed on *g*-C_3N_4 nanosheets. The total pore volume and the SSA was increased from 0.19 $cm^3 \cdot g^{-1}$ and 21.45 $m^2 \cdot g^{-1}$ of BCN to 0.66 $cm^3 \cdot g^{-1}$ and 87.99 $m^2 \cdot g^{-1}$ of CN-525, respectively. As nitrogen vacancies could cause the excitation of electrons into mid-gap states (−0.688 eV), and the electrons could be more easily excited from VB to mid-gap states than to CB. Relatively, with UV-visible absorption spectra, CN-525 exhibited an extended visible light absorption with a wide shoulder tail (450–700 nm). Therefore, the CN-525 photocatalyst displayed a remarkably higher photocatalytic H_2 evolution rate of 64.39 $\mu mol \cdot h^{-1}$, which was around 18 times over BCN.

4.2. CO_2 Reduction

Efficient photocatalytic conversion of CO_2 is vital to treat CO_2 emissions and generate beneficial chemicals and fuels. Photocatalytic CO_2 reduction has extremely complicated photocatalytic reaction mechanisms and pathways involving a proton-assisted multi-electron reduction process with high energy barriers, complex activation, and adsorption of CO_2 molecules. Due to the higher negative CB potential (−1.4 V), the photogenerated electrons of *g*-C_3N_4 works for reducing CO_2 into various products, such as HCOOH (−0.61 V),

CO (−0.53 V), HCHO (−0.48 V), CH_3OH (−0.38 V), and CH_4 (−0.24 V), vs. NHE. The pore structure makes *g*-C_3N_4 have an advantage in CO_2 adsorption. In seeking to advance the performance of porous *g*-C_3N_4, several approaches have been developed, for example, element doping and formation of heterojunctions with other semiconductors.

Heteroatom doping (e.g., B [199], P [200], S [201,202], O [203]) can alter the E_g, widen the visible light absorption, and boost the charge transfer efficiency to further enhance the photocatalytic CO_2 conversion properties in the visible-light region [204,205]. Wang et al., reported that CO_2 reduced to CH_3OH by the S-doped *g*-C_3N_4 photocatalyst with the rate of 1.12 $\mu mol \cdot g^{-1}$ compared to 0.81 $\mu mol \cdot g^{-1}$ of un-doped *g*-C_3N_4 [202]. In another case, porous P-doped *g*-C_3N_4 was obtained through the thermal reaction of melamine and sodium hypophosphite monohydrate ($NaH_2PO_2 \cdot H_2O$) (Figure 15a) [206]. The phosphine gas from the thermal decomposition of $NaH_2PO_2 \cdot H_2O$ induced mesopore structure of *g*-C_3N_4, giving a pore size of ~25 nm and SSA of 13.38 $m^2 \cdot g^{-1}$. Such mesoporous *g*-C_3N_4 showed a narrower E_g of 2.58 eV from 2.7 eV (Figure 15b), which was consistent with the wider absorption in 400–550 nm than pristine *g*-C_3N_4 (~450 nm). Owing to interstitial doping of P atom, there was an efficient electron-hole separation, as proved by a 2-times photocurrent increase. Therefore, the CO_2-to-CO and CO_2-to-CH_4 conversion rates reached 9.48 and 7.24 $\mu mol \cdot g^{-1}$ respectively, about 3.12 and 13.9 times higher than those on BCN (Figure 15c).

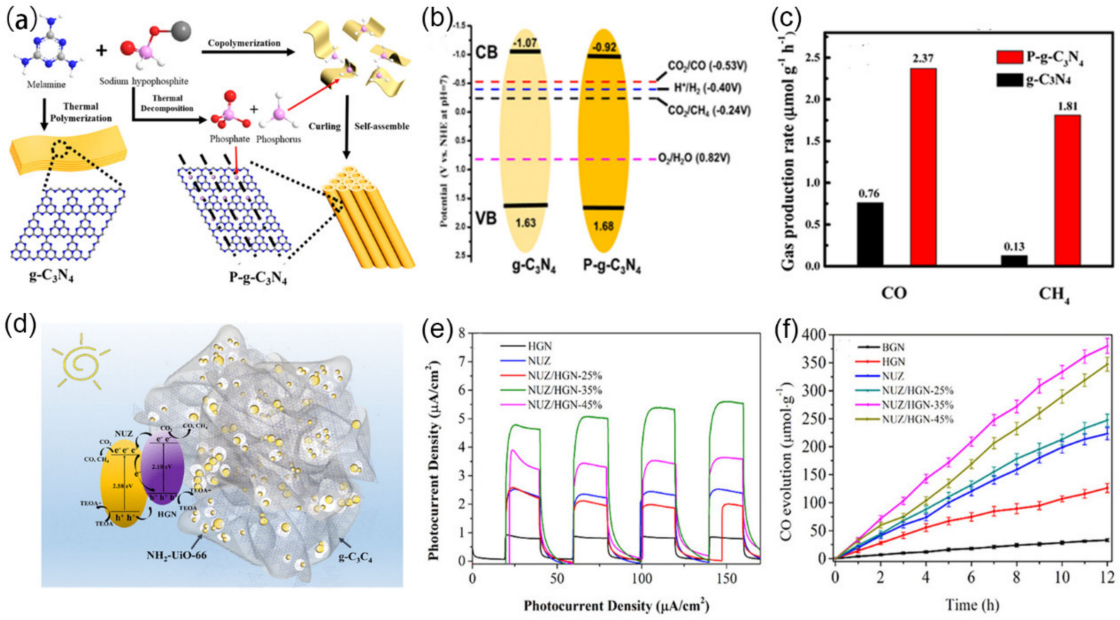

Figure 15. (**a**) Synthesis process of P-*g*-C_3N_4; (**b**) the electronic structure and all reaction reduction potentials of CO_2 conversion into CO and CH_4; (**c**) gas production rate of P-*g*-C_3N_4 and *g*-C_3N_4, Reprinted with permission from [206] 2018 American Chemistry Society; (**d**) The diagram of NUZ/HGN composites and diagram for energy band levels of NUZ/HGN composites; (**e**) photocurrent-time curves and (**f**) CO_2-to-CO conversion performance of HGN, NUZ, and NUZ/HGN under visible light irradiation, Reprinted with permission from [207] 2019 American Chemistry Society.

A series of porous *g*-C_3N_4-based heterostructures have been controllably designed and prepared based on the hybridizing strategy. So far, porous *g*-C_3N_4 was mainly combined with noble metals, semiconductors, carbons, and polymers, forming binary heterostructures. *g*-C_3N_4/semiconductor is a common class of heterogeneous nanostructures used for steering charge kinetics, extending the spectral range for light absorption and enhancing electron-hole separation [208]. OSCs have been widely studied on heterogenization with porous *g*-C_3N_4, mainly including dye sensitizers (e.g., porphyrin, phthalocyanine) [209], MOFs, COFs, etc. Especially for organic frameworks, their semiconductor characteristic

endows the composite heterostructure for efficient charge transportation, but also crystalline porous structures and extremely large SSA facilitates gas adsorption. Take MOFs as an example, the porous *g*-C_3N_4-based composites could achieve a larger surface area (1315.3 $m^2 \cdot g^{-1}$) and strong CO_2 capture (CO_2 uptake: 32.7 $cm^3 \cdot g^{-1}$) [210]. In another case, 3D holey *g*-C_3N_4 (HGN) was synthesized with melamine-cyanuric acid supramolecular as soft-template and melamine as precursor [207]. The prepared HGN was chemically bonded with NH_2-UiO-66(Zr) (NUZ) via rich-NHx and Zr-O clusters, yielding NUZ/HGN composites (SSA: 335 $m^2 \cdot g^{-1}$; pore volume: 0.2638 $cm^3 \cdot g^{-1}$) (Figure 15d). As the interfacial interaction would reallocate delocalized electrons among the π-conjugated networks of the HGN and NUZ, the enhancement of light-harvesting capability (200–800 nm) was observed. Besides, the interfacial charge transferring effect efficiently promoted the interfacial separation and migration efficiency of photogenerated charge carriers, as proved by the higher photocurrent density (Figure 15e). However, it was observed that NUZ could not well combine with HGN with the increase in HGN, according to the TEM image (Figure 5f). However, excessive HGN would stagger and overlap in the compound process through van der Waals interactions, which negatively affect the combination of NUZ and HGN and veil the active sites attached by NUZ. As a result, the NUZ/HGN-35% (35 wt.% of HCN) heterojunction showed the highest CO_2-to-CO conversion rate of 380 $\mu mol \cdot g^{-1}$ under light illumination for 12 h, which was much higher than that of HGN and NUZ (126 and 203 $\mu mol \cdot g^{-1}$) (Figure 15f).

4.3. Wastewater Treatment

Visible-light-driven wastewater treatment includes photooxidation reaction to degrade organic pollutants or inactivate bacteria, and photoreduction reaction for heavy metals removal. The CB position of *g*-C_3N_4 (−1.4 eV) is higher than the superoxide radical (O_2^-) production level ($O_2/\cdot O_2^-$, −0.33 eV vs. NHE) [211], such that the photogenerated electrons can reduce dissolved O_2 to strongly-oxidizing superoxide radical (O_2^-). The generated O_2^- species can react with electrons to form H_2O_2. Then, H_2O_2 reacts with electrons, forming hydroxyl radicals (OH). Associated with the behavior of the photogenerated carriers and the resonance energy transfer of excitons in polymer *g*-C_3N_4, singlet oxygen ($^1O_2$) can be generated [212]. The above reactive oxygen species (O_2^-, $^1O_2$, OH, and H_2O_2) generated by *g*-C_3N_4 are involved in the of organic pollutants degradation, including organic dyes (MB, MO, RhB, etc.), antibiotics (carbamazepine, tetracycline (TC), etc.), and organic compounds (phenol, oxalic acid, humic acid, etc.). Following a hole-dominant oxidative pathway, bacteria such as *Escherichiacoli* (*E. coli*) and *Staphylococcus aureus* (*S. aureus*) could be inactivated with an effective and recyclable porous *g*-C_3N_4 photocatalyst [213]. Besides photooxidation reaction on porous *g*-C_3N_4, the photoreduction for toxic heavy metal ion Cr(VI) or U(VI) has also been investigated [214]. So far, there are many reports that *g*-C_3N_4 was used as efficient photocatalysts in wastewater treatment.

Recently, developing 3D porous hydrogels or aerogels based on *g*-C_3N_4 is a potential approach to improving photocatalysts' wastewater treatment performance. Keeping *g*-C_3N_4 dispersing in gels prevents the stack between the *g*-C_3N_4 layers, which forms a highly porous and conductive network. On the one hand, the porous network provides abundant pathways for efficient charge migration, separation of photo-induced carriers, and hole diffusion, and enhances the contact between *g*-C_3N_4 and pollutants. On the other hand, the 3D structure makes the catalyst easy to recycle. Previously, several kinds of *g*-C_3N_4-based hydrogels or aerogels with enhanced wastewater treatment performance have been reported. Among them, *g*-C_3N_4/graphene or *g*-C_3N_4/graphene oxide hydrogels are the most widely studied because of the advanced mechanical properties and excellent electronic transmission performance of graphene. Besides, graphene hydrogel can quickly adsorb and enrich Cr ions because of the different modes of pore adsorption and surface adsorption. In one work, *g*-C_3N_4 nanosheets/reduced graphene hydrogel (*g*-C_3N_4/rGH) system was synthesized [215]. *g*-C_3N_4 nanosheets were uniformly dispersed in the 3D gel system, forming the pores with a diameter of about 3.9 nm and some mesopores (12.5–50 nm), giving

an SSA of 302.66 $m^2 \cdot g^{-1}$ (Figure 16a). On the one hand, the efficient removal of Cr(VI) is attributed to the high adsorption capacity of the porous network rGH. Results showed that 80% of Cr(VI) (30 $mg \cdot L^{-1}$) could be adsorbed by composite in the dark. However, the photoreduction ability of Cr(VI) was improved because of the decreased recombination of photo-generated electron-hole pairs brought by the excellent electronic transmission performance of reduced graphene. As PL results show in Figure 16b, there was a much lower intensity of *g*-C_3N_4/rGH than *g*-C_3N_4 nanosheets. Thanks to the synergistic effect of adsorption and photocatalysis, the removal of Cr(VI) reached 100% in 120 min under visible light irradiation via adsorption and photocatalysis (Figure 16c). The rate of treatment was 3.98 and 1.85-fold that of *g*-C_3N_4 nanosheets and rGH, respectively. At the same time, this hydrogel system with a micron-level structure was easily recyclable via a stainless-steel filter (pore size: ~38 μm), without the need to rely on a complex separation system, which maintained an 80% removal percentage of Cr(VI) after eight cycles (Figure 16d).

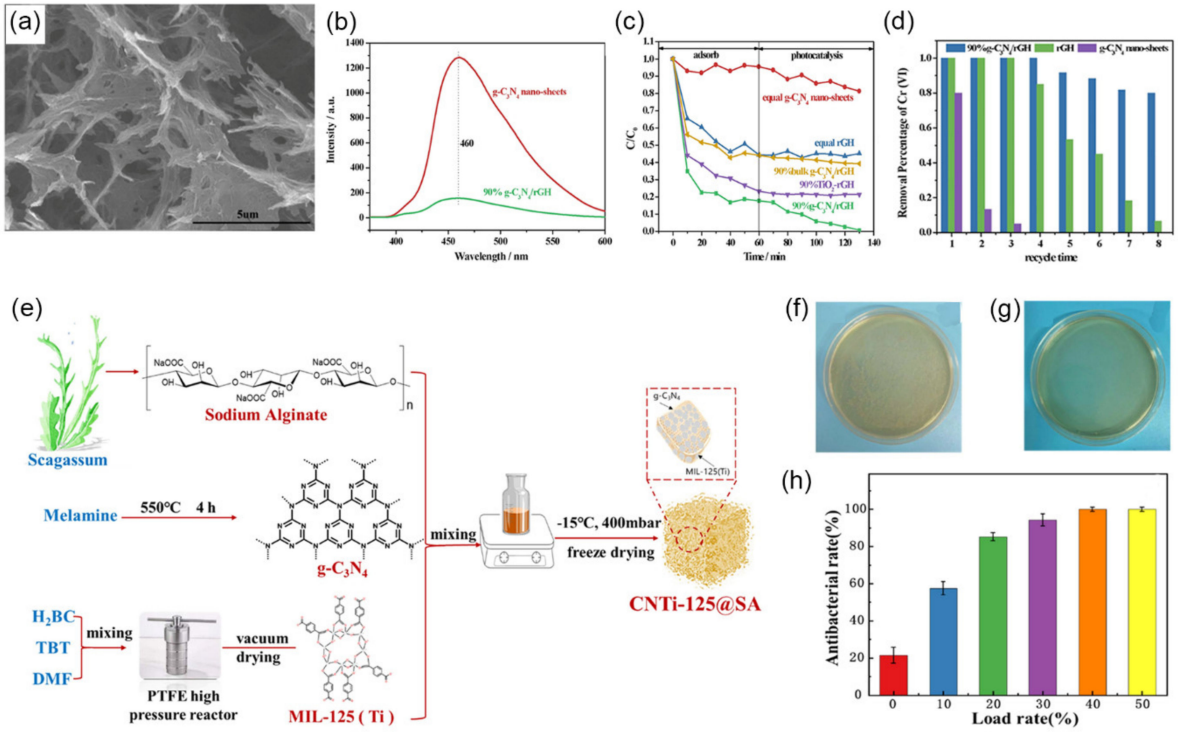

Figure 16. (**a**) SEM image of 90% *g*-C_3N_4/rGH; (**b**) PL spectra of *g*-C_3N_4 nanosheets, and 90% *g*-C_3N_4/rGH; (**c**) Cr(VI) adsorption capacity of different composite materials; (**d**) recycling runs of 90% *g*-C_3N_4/rGH in removing Cr(VI) without desorption, Reprinted with permission from [215] 2017 Elsevier; (**e**) Synthesis process of the CNTi-125@SA composite aerogels; antibacterial properties against *E. coli*: (**f**) blank control, (**g**) CNTi-125@SA; (**h**) antibacterial efficiency of the different composite aerogels, Reprinted with permission from [216] 2021 Elsevier.

Recently, the utilization of agar, konjac, and sodium alginate (SA) for preparing *g*-C_3N_4-based 3D porous gels was considered as a low-cost and eco-friendly strategy to solve the environmental crisis. In the organic pollutant degradation field, *g*-C_3N_4 nano-particle was first coated by agar uniformly, forming *g*-C_3N_4/agar hybrid hydrogels with a 3D mutual crosslinking network (pore size: 50 μm) by heating-cooling polymerization [217]. Via the synergistic effect of adsorption and photocatalysis, such hydrogels showed 1.3- and 4.5-times improvement of removing phenol and methylene, respectively. In another work, a konjac/*g*-C_3N_4 (KCN) aerogel was prepared by freeze-drying the hydrogel of *g*-C_3N_4 and konjac [218]. By forming the abundant porous channels (diameter about 200 μm), the O_2 could be rapidly delivered into the solution, which was a natural electron scavenger. As a result, the concentration of OH and $\cdot O_2^-$ increased, and the oxidation water treatment

process was boosted. To remove organic pollutants, the KCN could reach an MB removal of 97.90% and phenol removal of 99.34% in static states. The removal efficiency was kept at 100% in four cycles, indicating excellent cycle stability.

As for the application of antibacterial, Zhao et al., introduced *g*-C_3N_4/MIL-125(Ti) heterojunction into sodium alginate (SA), yielding *g*-C_3N_4/MIL-125 (Ti) @SA (CNTi-125@SA) composite aerogel after the freeze-drying process (Figure 16e) [216]. Numerous micropores ranging from 50 to 100 µm in size were caused by the astatic growth of ice crystals in the freezing process. The absorbed O_2 through a large number of pores reacted with MIL-125 (Ti) to generate $\cdot O_2^-$. Under visible light irradiation, the photogenerated holes were produced on *g*-C_3N_4. Organic *E. coli* tended to react with those highly oxidizing substances, eventually producing CO_2 and H_2O that completely inactivated the bacteria. The CNTi-125@SA aerogel exhibited an excellent antibacterial efficiency of 100% against *E. coli* (Figure 16f–h).

Photoelectrocatalytic (PEC) oxidation process using a semiconductor photoanode at a small positive potential has proven to be an efficient process for removing various pollutants from water. *g*-C_3N_4 has been recognized as promising for organics degradation, particularly in PEC application [219,220]. In one case, Liang et al., applied *g*-C_3N_4 electrode as the photoanode for phenol degradation [221]. Under visible light irradiation, the phenol could be depleted completely by the *g*-C_3N_4 with a 2.5 V bias, and 89.3% of the total organic carbon was removed. Recently, researchers utilized the PEC oxidation process of *g*-C_3N_4 to decompose noble metal-cyanide complexes and simultaneously recover noble metals from wastewaters [222]. A peroxymonosulfate/*g*-C_3N_4 nanosheet composites resulted in high Ag-cyanide decomposition and Ag recovery efficiencies (74% and 68%, respectively) within 150 min under visible light [223]. Semiconductors-based PEC technique has been proved to be an effective way to generate a synergistic effect for achieving H_2 evolution and organic pollutant degradation. The mechanistic pathway is that photogenerated electrons are transferred to the cathode for H_2 evolution under applied bias voltage, while organic compounds are degraded in the anode [224,225].

5. Conclusions

In general, *g*-C_3N_4, as an excellent photocatalyst, has a lot of development space in the field of photocatalysis in the future. *g*-C_3N_4 itself is non-toxic, pollution-free, and environmentally friendly. Pore structure endows *g*-C_3N_4 with a high SSA to provide more active sites, enhancing light absorption ability, photogenerated charges separation and transfer, and mass transfer for a redox reaction, thus greatly improving the photocatalytic performance. The construction and modification methods of *g*-C_3N_4 with a large SSA coordination pore structure have all been extensively researched in various photocatalytic applications. In this review, we first discussed the relationship between pore structure and photoelectric performance. We then reviewed three pore-modifying methods (hard-template, soft-template, and template-free methods) in detail. The advantages and disadvantages of each preparation method were emphasized and compared. Moreover, we also introduced recent achievements in pore structure *g*-C_3N_4 with the commonly used modification methods in photocatalytic fields, including water splitting, CO_2 reduction, and wastewater treatment. Overall, porous *g*-C_3N_4 as an excellent photocatalyst has a huge development space in photocatalysis in the future.

Although great progress has been made in researching porous *g*-C_3N_4 photocatalysts, several challenges remain. The improvement direction of the hard-template method is to simplify the preparation process and make it pollution-free. The research of the pore-modifying method transfers from hard-template method to soft-template method and template-free method because of the advantages, such as simple equipment, easy operation, and low cost. As for the soft-template and template-free methods, future development needs to pay more attention to designing the experimental scheme and selecting the precursors to alleviate interlayer collapse, interlayer stacking, and molecular polymerization to increase the SSA of the prepared samples. In addition, suitable functional modification

methods also play a significant role in tuning energy band structure and constructing interfacial electron transfer. However, the effect of the second component on the pore structure of *g*-C_3N_4 should be considered. Additionally, it is of great significance to develop large-scale applications of *g*-C_3N_4 photocatalysts in practical use. Since the performance of photocatalysts will be greatly reduced in real uncontrolled conditions and the deactivation will be faster in real environments, the performance testing conditions need to be more specific.

Author Contributions: Conceptualization, J.D. and Y.Z.; data curation, Y.Z. and W.Z.; writing—original draft preparation, J.D. and Y.Z.; writing—review and editing, J.D., M.I.H. and Y.C.; supervision, Y.C. and L.-N.W.; funding acquisition, L.-N.W. All authors have read and agreed to the published version of the manuscript.

Funding: Scientific and Technological Innovation Foundation of Shunde Graduate School, USTB (BK19AE027; BK20BE022).

Institutional Review Board Statement: Not applicable.

Informed Consent Statement: Not applicable.

Data Availability Statement: Not applicable.

Conflicts of Interest: The authors declare no conflict of interest.

References

1. Chen, Y.; Li, A.; Li, Q.; Hou, X.; Wang, L.-N.; Huang, Z.-H. Facile Fabrication of Three-Dimensional Interconnected Nanoporous N-TiO_2 for Efficient Photoelectrochemical Water Splitting. *J. Mater. Sci. Technol.* **2018**, *34*, 955–960. [CrossRef]
2. Osterloh, F.E. Inorganic Nanostructures for Photoelectrochemical and Photocatalytic Water Splitting. *Chem. Soc. Rev.* **2013**, *42*, 2294–2320. [CrossRef] [PubMed]
3. Chen, Y.-Z.; Li, W.-H.; Li, L.; Wang, L.-N. Progress in Organic Photocatalysts. *Rare Met.* **2018**, *37*, 1–12. [CrossRef]
4. Chen, B.; Yu, J.; Wang, R.; Zhang, X.; He, B.; Jin, J.; Wang, H.; Gong, Y. Three-Dimensional Ordered Macroporous g-C_3N_4-Cu_2O-TiO_2 Heterojunction for Enhanced Hydrogen Production. *Sci. China Mater.* **2021**, *6*, 1–8. [CrossRef]
5. Chen, M.; Bai, R.; Jin, P.; Li, J.; Yan, Y.; Peng, A.; He, J. A Facile Hydrothermal Synthesis of Few-Layer Oxygen-Doped g-C_3N_4 with Enhanced Visible Light-Responsive Photocatalytic Activity. *J. Alloy. Compd.* **2021**, *869*, 159292. [CrossRef]
6. Chen, Z.; Zhang, S.; Liu, Y.; Alharbi, N.S.; Rabah, S.O.; Wang, S.; Wang, X. Synthesis and Fabrication of g-C_3N_4-Based Materials and Their Application in Elimination of Pollutants. *Sci. Total Environ.* **2020**, *731*, 139054. [CrossRef]
7. Cheng, F.; Yin, H.; Xiang, Q. Low-Temperature Solid-State Preparation of Ternary CdS/g-C_3N_4/CuS Nanocomposites for Enhanced Visible-Light Photocatalytic H_2 Production Activity. *Appl. Surf. Sci.* **2017**, *391*, 432–439. [CrossRef]
8. Han, C.; Su, P.; Tan, B.; Ma, X.; Lv, H.; Huang, C.; Wang, P.; Tong, Z.; Li, G.; Huang, Y.; et al. Defective Ultra-Thin Two-Dimensional g-C_3N_4 Photocatalyst for Enhanced Photocatalytic H_2 Evolution Activity. *J. Colloid Interface Sci.* **2021**, *581*, 159–166. [CrossRef]
9. Das, K.K.; Patnaik, S.; Mansingh, S.; Behera, A.; Mohanty, A.; Acharya, C.; Parida, K.M. Enhanced Photocatalytic Activities of Polypyrrole Sensitized Zinc Ferrite/Graphitic Carbon Nitride n-n Heterojunction towards Ciprofloxacin Degradation, Hydrogen Evolution and Antibacterial Studies. *J. Colloid Interface Sci.* **2020**, *561*, 551–567. [CrossRef]
10. Mohamed, F.; Abukhadra, M.R.; Shaban, M. Removal of Safranin Dye from Water Using Polypyrrole Nanofiber/Zn-Fe Layered Double Hydroxide Nanocomposite (Ppy NF/Zn-Fe LDH) of Enhanced Adsorption and Photocatalytic Properties. *Sci. Total Environ.* **2018**, *640*, 352–363. [CrossRef]
11. Deng, X.; Chen, Y.; Wen, J.; Xu, Y.; Zhu, J.; Bian, Z. Polyaniline-TiO_2 Composite Photocatalysts for Light-Driven Hexavalent Chromium Ions Reduction. *Sci. Bull.* **2020**, *65*, 105–112. [CrossRef]
12. Eskizeybek, V.; Sari, F.; Gulce, H.; Gulce, A.; Avci, A. Preparation of the New Polyaniline/ZnO Nanocomposite and Its Photocatalytic Activity for Degradation of Methylene Blue and Malachite Green Dyes under UV and Natural Sun Lights Irradiations. *Appl. Catal. B Environ.* **2012**, *119*, 197–206. [CrossRef]
13. Zhang, K.; Li, H.; Shi, H.; Hong, W. Polyimide with Enhanced π Stacking for Efficient Visible-Light-Driven Photocatalysis. *Catal. Sci. Technol.* **2021**, *11*, 4889–4897. [CrossRef]
14. Bao, H.; Chen, X.; Yuan, R.; Zhang, C.; Xu, S. A Dual Polymer Composite of Poly (3-Hexylthiophene) and Poly (3,4-Ethylenedioxythiophene) Hybrid Surface Heterojunction with g-C_3N_4 for Enhanced Photocatalytic Hydrogen Evolution. *RSC Adv.* **2021**, *11*, 32671–32679. [CrossRef]
15. Tremblay, P.-L.; Xu, M.; Chen, Y.; Zhang, T. Nonmetallic Abiotic-Biological Hybrid Photocatalyst for Visible Water Splitting and Carbon Dioxide Reduction. *iScience* **2020**, *23*, 100784. [CrossRef]
16. Xu, M.; Tremblay, P.-L.; Jiang, L.; Zhang, T. Stimulating Bioplastic Production with Light Energy by Coupling Ralstonia Eutropha with the Photocatalyst Graphitic Carbon Nitride. *Green Chem.* **2019**, *21*, 2392–2400. [CrossRef]

17. Chen, Z.; Zheng, B.; Li, X.; Fu, M.; Xie, S.; Deng, C.; Hu, Y. Progress in the Preparation of Nanomaterials Employing Template Method. *Chem. Ind. Eng. Prog.* **2010**, *29*, 94–99. [CrossRef]
18. Zhou, Z.; Zhang, Y.; Shen, Y.; Liu, S.; Zhang, Y. Molecular engineering of polymeric carbon nitride: Advancing applications from photocatalysis to biosensing and more. *Chem. Soc. Rev.* **2018**, *47*, 2298–2321. [CrossRef]
19. Wu, C.; Xue, S.; Qin, Z.; Nazari, M.; Yang, G.; Yue, S.; Tong, T.; Ghasemi, H.; Hernandez, F.C.R.; Xue, S.; et al. Making g-C3N4 ultra-thin nanosheets active for photocatalytic overall water splitting. *Appl. Catal. B Environ.* **2021**, *282*, 119557. [CrossRef]
20. Tian, B.; Wu, Y.; Lu, G. Metal-Free Plasmonic Boron Phosphide/Graphitic Carbon Nitride with Core-Shell Structure Photocatalysts for Overall Water Splitting. *Appl. Catal. B Environ.* **2021**, *280*, 119410. [CrossRef]
21. Zhao, H.; Jiang, Z.; Xiao, K.; Sun, H.; Chan, H.S.; Tsang, T.H.; Yang, S.; Wong, P.K. Photo-Assisted Separation of Noble-Metal-Free Oxidation and Reduction Cocatalysts for Graphitic Carbon Nitride Nanosheets with Efficient Photocatalytic Hydrogen Evolution. *Appl. Catal. B Environ.* **2021**, *280*, 119456. [CrossRef]
22. Gu, J.-W.; Guo, R.-T.; Miao, Y.-F.; Liu, Y.-Z.; Wu, G.-L.; Duan, C.-P.; Pan, W.-G. Construction of Full Spectrum-Driven $CsxWO_3$/g-C_3N_4 Heterojunction Catalyst for Efficient Photocatalytic CO_2 Reduction. *Appl. Surf. Sci.* **2021**, *540*, 148316. [CrossRef]
23. Li, L.; Zhang, Z.; Ding, C.; Xu, J. Boosting Charge Separation and Photocatalytic CO_2 Reduction of $CsPbBr_3$ Perovskite Quantum Dots by Hybridizing with P_3HT. *Chem. Eng. J.* **2021**, *419*, 129543. [CrossRef]
24. Wang, X.; Li, Q.; Gan, L.; Ji, X.; Chen, F.; Peng, X.; Zhang, R. 3D Macropore Carbon-Vacancy g-C_3N_4 Constructed Using Polymethylmethacrylate Spheres for Enhanced Photocatalytic H_2 Evolution and CO_2 Reduction. *J. Energy Chem.* **2021**, *53*, 139–146. [CrossRef]
25. Liu, R.; Bie, Y.; Qiao, Y.; Liu, T.; Song, Y. Design of g-C_3N_4/TiO_2 Nanotubes Heterojunction for Enhanced Organic Pollutants Degradation in Waste Water. *Mater. Lett.* **2019**, *251*, 126–130. [CrossRef]
26. Chen, W.; Liu, M.; Wei, S.; Li, X.; Mao, L.; Shangguan, W. Solid-State Synthesis of Ultrathin MoS_2 as a Cocatalyst on Mesoporous g-C_3N_4 for Excellent Enhancement of Visible Light Photoactivity. *J. Alloy. Compd.* **2020**, *836*, 155401. [CrossRef]
27. Wu, M.; Yan, J.-M.; Zhang, X.-W.; Zhao, M. Synthesis of g-C_3N_4 with Heating Acetic Acid Treated Melamine and Its Photocatalytic Activity for Hydrogen Evolution. *Appl. Surf. Sci.* **2015**, *354*, 196–200. [CrossRef]
28. Zhao, S.; Zhang, Y.; Zhou, Y.; Wang, Y.; Qiu, K.; Zhang, C.; Fang, J.; Sheng, X. Facile One-Step Synthesis of Hollow Mesoporous g-C_3N_4 Spheres with Ultrathin Nanosheets for Photoredox Water Splitting. *Carbon* **2018**, *126*, 247–256. [CrossRef]
29. Wang, X.-Y.; Wang, Y.; Zhao, N.-D.; Zheng, M.; Guo, Y.-R.; Pan, Q.-J. Van Der Waals Enhanced Interfacial Interaction in Cellulose/Zinc Oxide Nanocomposite Coupled by Graphitic Carbon Nitride. *Carbohydr. Polym.* **2021**, *268*, 118235. [CrossRef]
30. Liang, Q.; Li, Z.; Yu, X.; Huang, Z.-H.; Kang, F.; Yang, Q.-H. Macroscopic 3D Porous Graphitic Carbon Nitride Monolith for Enhanced Photocatalytic Hydrogen Evolution. *Adv. Mater.* **2015**, *27*, 4634–4639. [CrossRef]
31. Li, Y.; Liu, Z.; Li, Z.; Wang, Q. Renewable Biomass-Derived Carbon-Supported g-C_3N_4 Doped with Ag for Enhanced Photocatalytic Reduction of CO_2. *J. Colloid Interface Sci.* **2022**, *606*, 1311–1321. [CrossRef] [PubMed]
32. Kumar, A.; Kashyap, S.; Sharma, M.; Krishnan, V. Tuning the Surface and Optical Properties of Graphitic Carbon Nitride by Incorporation of Alkali Metals (Na, K, Cs and Rb): Effect on Photocatalytic Removal of Organic Pollutants. *Chemosphere* **2022**, *287*, 131988. [CrossRef] [PubMed]
33. Wang, Y.; Wang, H.; Chen, F.; Cao, F.; Zhao, X.; Meng, S.; Cui, Y. Facile Synthesis of Oxygen Doped Carbon Nitride Hollow Microsphere for Photocatalysis. *Appl. Catal. B Environ.* **2017**, *206*, 417–425. [CrossRef]
34. Guo, S.; Tang, Y.; Xie, Y.; Tian, C.; Feng, Q.; Zhou, W.; Jiang, B. P-doped Tubular g-C_3N_4 with Surface Carbon Defects: Universal Synthesis and Enhanced Visible-Light Photocatalytic Hydrogen Production. *Appl. Catal. B Environ.* **2017**, *218*, 664–671. [CrossRef]
35. Yang, Y.; Zhang, C.; Huang, D.; Zeng, G.; Huang, J.; Lai, C.; Zhou, C.; Wang, W.; Guo, H.; Xue, W.; et al. Boron Nitride Quantum Dots Decorated Ultrathin Porous g-C_3N_4: Intensified Exciton Dissociation and Charge Transfer for Promoting Visible-Light-Driven Molecular Oxygen Activation. *Appl. Catal. B Environ.* **2019**, *245*, 87–99. [CrossRef]
36. Wen, J.; Xie, J.; Yang, Z.; Shen, R.; Li, H.; Luo, X.; Chen, X.; Li, X. Fabricating the Robust g-C_3N_4 Nanosheets/Carbons/NiS Multiple Heterojunctions for Enhanced Photocatalytic H_2 Generation: An Insight into the Trifunctional Roles of Nanocarbons. *ACS Sustain. Chem. Eng.* **2017**, *5*, 2224–2236. [CrossRef]
37. Arunraj, B.; Kaushik, U.S.G.; Rajesh, V.; Rajesh, N. Combinative Influence of Graphitic Carbon Nitride and Halomonas BVR1Bacteria Augment the Adsorptive Recovery of Precious 'Euro'pium. *Chem. Eng. J.* **2021**, *404*, 126466. [CrossRef]
38. Wei, F.; Kuang, S.; Rees, T.W.; Liao, X.; Liu, J.; Luo, D.; Wang, J.; Zhang, X.; Ji, L.; Chao, H. Ruthenium(II) Complexes Coordinated to Graphitic Carbon Nitride: Oxygen Self-Sufficient Photosensitizers Which Produce Multiple ROS for Photodynamic Therapy in Hypoxia. *Biomaterials* **2021**, *276*, 121064. [CrossRef]
39. Sun, X.; An, X.; Zhang, S.; Li, Z.; Zhang, J.; Wu, W.; Wu, M. Physical Vapor Deposition (PVD): A Method to Fabricate Modified g-C_3N_4 Sheets. *New J. Chem.* **2019**, *43*, 6683–6687. [CrossRef]
40. Wang, Y.; Wang, F.; Zuo, Y.; Zhang, X.; Cui, L.-F. Simple Synthesis of Ordered Cubic Mesoporous Graphitic Carbon Nitride by Chemical Vapor Deposition Method Using Melamine. *Mater. Lett.* **2014**, *136*, 271–273. [CrossRef]
41. Cao, M.; Wang, K.; Tudela, I.; Fan, X. Improve Photocatalytic Performance of g-C_3N_4 through Balancing the Interstitial and Substitutional Chlorine Doping. *Appl. Surf. Sci.* **2021**, *536*, 147784. [CrossRef]
42. Zhou, J.; Ding, J.; Wan, H.; Guan, G. Boosting Photocatalytic Degradation of Antibiotic Wastewater by Synergy Effect of Heterojunction and Phosphorus Soping. *J. Colloid Interface Sci.* **2021**, *582*, 961–968. [CrossRef]

43. Zhang, B.; Shi, H.; Yan, Y.; Liu, C.; Hu, X.; Liu, E.; Fan, J. A Novel S-Scheme 1D/2D Bi_2S_3/g-C_3N_4 Heterojunctions with Enhanced H_2 Evolution Activity. *Colloid Surf. A Physicochem. Eng. Asp.* **2021**, *608*, 125598. [CrossRef]
44. Barrio, J.; Grafmueller, A.; Tzadikov, J.; Shalom, M. Halogen-Hydrogen Bonds: A General Synthetic Approach for Highly Photoactive Carbon Nitride with Tunable Properties. *Appl. Catal. B Environ.* **2018**, *237*, 681–688. [CrossRef]
45. Trangwachirachai, K.; Chen, C.-H.; Huang, A.-L.; Lee, J.-F.; Chen, C.-L.; Lin, Y.-C. Conversion of Methane to Acetonitrile over GaN Catalysts Derived from Gallium Nitrate Hydrate Co-Pyrolyzed with Melamine, Melem, or g-C_3N_4: The Influence of Nitrogen Precursors. *Catal. Sci. Technol.* **2021**. [CrossRef]
46. Wang, Y.; Wang, X.; Antonietti, M.; Zhang, Y. Facile One-Pot Synthesis of Nanoporous Carbon Nitride Solids by Using Soft Templates. *ChemSusChem* **2010**, *3*, 435–439. [CrossRef]
47. Ji, H.; Chang, F.; Hu, X.; Qin, W.; Shen, J. Photocatalytic degradation of 2,4,6-trichlorophenol over g-C_3N_4 under visible light irradiation. *Chem. Eng. J.* **2013**, *218*, 183–190. [CrossRef]
48. Yan, S.C.; Li, Z.S.; Zou, Z.G. Photodegradation Performance of g-C_3N_4 Fabricated by Directly Heating Melamine. *Langmuir* **2009**, *25*, 10397–10401. [CrossRef]
49. Zhang, Y.; Liu, J.; Wu, G.; Chen, W. Porous graphitic carbon nitride synthesized via direct polymerization of urea for efficient sunlight-driven photocatalytic hydrogen production. *Nanoscale* **2012**, *4*, 5300–5303. [CrossRef]
50. Zhang, G.; Zhang, J.; Zhang, M.; Wang, X. Polycondensation of thiourea into carbon nitride semiconductors as visible light photocatalysts. *J. Mater. Chem.* **2012**, *22*, 8083–8091. [CrossRef]
51. Cheng, M.; Lv, P.; Zhang, X.; Xiong, R.; Guo, Z.; Wang, Z.; Zhou, Z.; Zhang, M. A New Active Species of Pd-N-x Synthesized by Hard-Template Method for Efficiently Catalytic Hydrogenation of Nitroarenes. *J. Catal.* **2021**, *399*, 182–191. [CrossRef]
52. Wang, L.; Zhang, W.; Su, Y.; Liu, Z.; Du, C. Halloysite Derived 1D Mesoporous Tubular g-C_3N_4: Synergy of Template Effect and Associated Carbon for Boosting Photocatalytic Performance toward Tetracycline Removal. *Appl. Clay Sci.* **2021**, *213*, 106238. [CrossRef]
53. Huang, X.; Zhang, Y.; Lai, Y.; Li, Y. Mesoporous Graphitic Carbon Nitride for Adsorptive Desulfurization in an Isooctane Solution. *J. Sulfur Chem.* **2021**, *10*, 1985120. [CrossRef]
54. Jiang, T.; Han, H.; Dong, M.; Zhao, Q. In Situ Construction of Porous g-C_3N_4 Isotype Heterojunction/BiOBr Nanosheets Ternary Composite Catalyst for Highly Efficient Visible-Light Photocatalytic Activity. *ChemistrySelect* **2021**, *6*, 6212–6222. [CrossRef]
55. Ai, L.; Fan, H. CTAB-Melamine Molecular Crystals as Precursor for Synthesis of Layered Carbon Nitride Porous Nanostructures with Enhanced Photocatalytic Activity for Hydrogen Production. *Mater. Today Commun.* **2021**, *29*, 102780. [CrossRef]
56. Li, H.; Ning, F.; Chen, X.; Shi, A. Effect of Carbon and Nitrogen Double Vacancies on the Improved Photocatalytic Hydrogen Evolution over Porous Carbon Nitride Nanosheets. *Catal. Sci. Technol.* **2021**, *11*, 3270–3278. [CrossRef]
57. Liang, Z.; Liu, L.; Zhuang, X.; Tang, Z.; Li, H.; Kang, W. Polyhedral Oligomeric Silsesquioxane as a Recyclable Soft Template to Synthesize Mesoporous Polymeric Carbon Nitride with Enhanced Photocatalytic Hydrogen Evolution. *Sustain. Energy Fuels* **2021**, *5*, 112–116. [CrossRef]
58. Deng, P.; Hong, W.; Cheng, Z.; Zhang, L.; Hou, Y. Facile Fabrication of Nickel/Porous g-C_3N_4 by Using Carbon Dot as Template for Enhanced Photocatalytic Hydrogen Production. *Int. J. Hydrog. Energy* **2020**, *45*, 33543–33551. [CrossRef]
59. Yu, Y.; Xu, W.; Fang, J.; Chen, D.; Pan, T.; Feng, W.; Liang, Y.; Fang, Z. Soft-Template Assisted Construction of Superstructure TiO_2/SiO_2/g-C_3N_4 Hybrid as Efficient Visible-Light Photocatalysts to Degrade Berberine in Seawater via an Adsorption-Photocatalysis Synergy and Mechanism Insight. *Appl. Catal. B Environ.* **2020**, *268*, 118751. [CrossRef]
60. Sharma, P.; Sarngan, P.P.; Lakshmanan, A.; Sarkar, D. One-step Synthesis of Highly Reactive g-C_3N_4. *J. Mater. Sci. Mater. Electron.* **2021**, *10*, 1–10. [CrossRef]
61. Yang, X.; Cao, G.; Liu, H.; Wang, C.; Li, X.; Song, Z. Construction of Nesoporous C_3N_4/rGO Composite with Enhanced Visible Light Photocatalytic Activity. *Optik* **2021**, *241*, 167159. [CrossRef]
62. Phoon, B.L.; Lai, C.W.; Pan, G.-T.; Yang, T.C.K.; Juan, J.C. Highly Mesoporous g-C_3N_4 with Uniform Pore Size Distribution via the Template-Free Method to Enhanced Solar-Driven Tetracycline Degradation. *Nanomaterials* **2021**, *11*, 2041. [CrossRef] [PubMed]
63. Zhang, M.; Sun, Y.; Chang, X.; Zhang, P. Template-Free Synthesis of One-Dimensional g-C_3N_4 Chain Nanostructures for Efficient Photocatalytic Hydrogen Evolution. *Front. Chem.* **2021**, *9*, 652762. [CrossRef] [PubMed]
64. Davis, M.E. Ordered Porous Materials for Merging Applications. *Nature* **2002**, *417*, 813–821. [CrossRef]
65. Fang, Z.; Bueken, B.; De Vos, D.E.; Fischer, R.A. Defect-Engineered Metal-Organic Frameworks. *Angew. Chem. Int. Ed.* **2015**, *54*, 7234–7254. [CrossRef]
66. Razavi, M.; Bordonaro, G.G.; Ferro, P.; Torgersen, J.; Berto, F. Porosity Effect on Tensile Behavior of Ti-6Al-4V Specimens Produced by Laser Engineered Net Shaping Technology. *Proc. Inst. Mech. Eng. C J. Mech. Eng. Sci.* **2018**, *235*, 1989–1996. [CrossRef]
67. Tatarchuk, T.; Myslin, M.; Mironyuk, I.; Bououdina, M.; Pędziwiatr, A.T.; Gargula, R.; Bogacz, B.F.; Kurzydło, P. Synthesis, Morphology, Crystallite Size and Adsorption Properties of Nanostructured Mg-Zn Ferrites with Enhanced Porous Structure. *J. Alloy. Compd.* **2020**, *819*, 152945. [CrossRef]
68. Zou, K.; Cai, P.; Wang, B.; Liu, C.; Li, J.; Qiu, T.; Zou, G.; Hou, H.; Ji, X. Insights into Enhanced Capacitive Behavior of Carbon Cathode for Lithium Ion Capacitors: The Coupling of Pore Size and Graphitization Engineering. *Nano-Micro Lett.* **2020**, *12*, 121. [CrossRef]

69. Garcia-Mulero, A.; Rendon-Patino, A.; Asiri, A.M.; Primo, A.; Garcia, H. Band Engineering of Semiconducting Microporous Graphitic Carbons by Phosphorous Doping: Enhancing of Photocatalytic Overall Water Splitting. *ACS Appl. Mater. Interfaces* **2021**, *13*, 48753–48763. [CrossRef]
70. Wang, D.; Jia, F.; Wang, H.; Chen, F.; Fang, Y.; Dong, W.; Zeng, G.; Li, X.; Yang, Q.; Yuan, X. Simultaneously Efficient Adsorption and Photocatalytic Degradation of Tetracycline by Fe-Based MOFs. *J. Colloid Interface Sci.* **2018**, *519*, 273–284. [CrossRef]
71. Tian, N.; Zhang, Y.; Li, X.; Xiao, K.; Du, X.; Dong, F.; Waterhouse, G.I.N.; Zhang, T.; Huang, H. Precursor-Reforming Protocol to 3D Mesoporous g-C_3N_4 Established by Ultrathin Self-Doped Nanosheets for Superior Hydrogen Evolution. *Nano Energy* **2017**, *38*, 72–81. [CrossRef]
72. Xiong, C.; Li, B.; Lin, X.; Liu, H.; Xu, Y.; Mao, J.; Duan, C.; Li, T.; Ni, Y. The Recent Progress on Three-dimensional Porous Graphene-Based Hybrid Structure for Supercapacitor. *Compos. Part B Eng.* **2019**, *165*, 10–46. [CrossRef]
73. Zhao, X.; Pachfule, P.; Li, S.; Langenhahn, T.; Ye, M.; Schlesiger, C.; Praetz, S.; Schmidt, J.; Thomas, A. Macro/Microporous Covalent Organic Frameworks for Efficient Electrocatalysis. *J. Am. Chem. Soc.* **2019**, *141*, 6623–6630. [CrossRef]
74. Chen, X.; Jiang, X.; Yin, C.; Zhang, B.; Zhang, Q. Facile Fabrication of Hierarchical Porous ZIF-8 for Enhanced Adsorption of Antibiotics. *J. Hazard. Mater.* **2019**, *367*, 194–204. [CrossRef]
75. Li, Y.; Jin, R.; Xing, Y.; Li, J.; Song, S.; Liu, X.; Li, M.; Jin, R. Macroscopic Foam-Like Holey Ultrathin g-C_3N_4 Nanosheets for Drastic Improvement of Visible-Light Photocatalytic Activity. *Adv. Energy Mater.* **2016**, *6*, 1601273. [CrossRef]
76. Fang, B.; Kim, J.H.; Kim, M.-S.; Yu, J.-S. Hierarchical Nanostructured Carbons with Meso–Macroporosity: Design, Characterization, and Applications. *ACS Appl. Mater. Interfaces* **2013**, *46*, 1397–1406. [CrossRef]
77. Zhang, Y.; Jiang, H.; Wang, Q.; Meng, C. In-Situ Hydrothermal Growth of $Zn_4Si_2O_7(OH)_2{\cdot}H_2O$ Anchored on 3D N, S-Enriched Carbon Derived from Plant Biomass for Flexible Solid-state Asymmetrical Supercapacitors. *Chem. Eng. J.* **2018**, *352*, 519–529. [CrossRef]
78. Yang, X.-Y.; Chen, L.-H.; Li, Y.; Rooke, J.C.; Sanchez, C.; Su, B.-L. Hierarchically Porous Materials: Synthesis Strategies and Structure Design. *Chem. Soc. Rev.* **2017**, *46*, 481–558. [CrossRef]
79. Li, L.; Xiang, S.; Cao, S.; Zhang, J.; Ouyang, G.; Chen, L.; Su, C.-Y. A Synthetic Route to Ultralight Hierarchically Micro/Mesoporous Al(III)-Carboxylate Metal-Organic Aerogels. *Nat. Commun.* **2013**, *4*, 1774–1783. [CrossRef]
80. Hao, R.; Wang, G.; Tang, H.; Sun, L.; Xu, C.; Han, D. Template-Free Preparation of Macro/Mesoporous g-C_3N_4/TiO_2 Teterojunction Photocatalysts with Enhanced Visible Light Photocatalytic Activity. *Appl. Catal. B Environ.* **2016**, *187*, 47–58. [CrossRef]
81. Wei, J.; Chen, Y.; Zhang, H.; Zhuang, Z.; Yu, Y. Hierarchically Porous S-Scheme CdS/UiO-66 Photocatalyst for Efficient 4-Nitroaniline Reduction. *Chin. J. Catal.* **2021**, *42*, 78–86. [CrossRef]
82. Dong, G.; Zhang, Y.; Pan, Q.; Qiu, J. A Fantastic Graphitic Carbon Nitride (g-C_3N_4) Material: Electronic Structure, Photocatalytic and Photoelectronic Properties. *J. Photochem. Photobiol. C Photochem. Rev.* **2014**, *20*, 33–50. [CrossRef]
83. Zhao, H.-M.; Di, C.-M.; Wang, L.; Chun, Y.; Xu, Q.-H. Synthesis of Mesoporous Graphitic C_3N_4 Using Cross-Linked Bimodal Mesoporous SBA-15 as a Hard Template. *Microporous Mesoporous Mater.* **2015**, *208*, 98–104. [CrossRef]
84. Wang, W.; Fang, J.; Chen, H. Nano-Confined g-C_3N_4 in Mesoporous SiO_2 with Improved Quantum Size Effect and Tunable Structure for Photocatalytic Tetracycline Antibiotic Degradation. *J. Alloy. Compd.* **2020**, *819*, 153064. [CrossRef]
85. Li, Y.; Qu, W.; Huang, L.; Li, P.; Zhang, F.; Yuan, D.; Wang, Q.; Xu, H.; Li, H. Porous-C_3N_4 with High Ability for Selective Adsorption and Photodegradation of Dyes Under Visible-Light. *J. Inorg. Organomet. Polym. Mater.* **2017**, *27*, 1674–1682. [CrossRef]
86. Hong, Y.; Liu, E.; Shi, J.; Lin, X.; Sheng, L.; Zhang, M.; Wang, L.; Chen, J. A Direct One-Step Synthesis of Ultrathin g-C_3N_4 Nanosheets from Thiourea for Boosting Solar Photocatalytic H_2 Evolution. *Int. J. Hydrog. Energy* **2019**, *44*, 7194–7204. [CrossRef]
87. Wang, J.; Wang, Y.; Wang, W.; Ding, Z.; Geng, R.; Li, P.; Pan, D.; Liang, J.; Qin, H.; Fan, Q. Tunable Mesoporous g-C_3N_4 Nanosheets as a Metal-Free Catalyst for Enhanced Visible-Light-Driven Photocatalytic Reduction of U(VI). *Chem. Eng. J.* **2020**, *383*, 123193. [CrossRef]
88. Jiang, T.S.; Du, Y.; Dong, M.F.; Zhao, Q. The facile synthesis and enhanced photocatalytic activity of a graphitic carbon nitride isotype heterojunction with ordered mesopores. *New J. Chem.* **2019**, *43*, 10915–10925. [CrossRef]
89. Liu, H.J.; Wu, H.N.; Lv, J.; Xu, G.Q.; Chen, X.; Zhang, X.Y.; Wu, Y.C. SBA-15 Templated Mesoporous Graphitic C_3N_4 for Remarkably Enhanced Photocatalytic Degradation of Organic Pollutants under Visible Light. *Nano* **2019**, *14*, 19501364. [CrossRef]
90. Obregon, S.; Vazquez, A.; Ruiz-Gomez, M.A.; Rodriguez-Gonzalez, V. SBA-15 assisted preparation of mesoporous g-C_3N_4 for photocatalytic H_2 production and Au^{3+} fluorescence sensing. *Appl. Surf. Sci.* **2019**, *488*, 205–212. [CrossRef]
91. Gao, X.C.; Jiao, X.J.; Zhang, L.C.; Zhu, W.C.; Xu, X.H.; Ma, H.Y.; Chen, T. Cosolvent-free nanocasting synthesis of ordered mesoporous g-C_3N_4 and its remarkable photocatalytic activity for methyl orange degradation. *RSC Adv.* **2015**, *5*, 76963–76972. [CrossRef]
92. Li, X.B.; Masters, A.F.; Maschmeyer, T. Photocatalytic Hydrogen Evolution from Silica-Templated Polymeric Graphitic Carbon Nitride-Is the Surface Area Important? *ChemCatChem* **2015**, *7*, 121–126. [CrossRef]
93. Liu, J.Y.; Yan, J.; Ji, H.Y.; Xu, Y.G.; Huang, L.Y.; Li, Y.P.; Song, Y.H.; Zhang, Q.; Xu, H.; Li, H.M. Controlled synthesis of ordered mesoporous g-C_3N_4 with a confined space effect on its photocatalytic activity. *Mater. Sci. Semicond. Process* **2016**, *46*, 59–68. [CrossRef]
94. Ovcharov, M.; Shcherban, N.; Filonenko, S.; Mishura, A.; Skoryk, M.; Shvalagin, V.; Granchak, V. Hard template synthesis of porous carbon nitride materials with improved efficiency for photocatalytic CO_2 utilization. *Mater. Sci. Eng. B* **2015**, *202*, 1–7. [CrossRef]

95. Esmati, M.; Allahresani, A.; Naghizadeh, A. Synthesis and characterization of Graphitic Carbon Nitride/Mesoporous Nano-Silica (g-C_3N_4/KCC-1) nanocomposite as a novel highly efficient and recyclable photocatalyst for degradation of antibiotic in aqueous solution. *Res. Chem. Intermed.* **2021**, *47*, 1447–1469. [CrossRef]
96. Kadi, M.W.; Mohamed, R.M.; Ismail, A.A.; Bahnemann, D.W. Soft and hard templates assisted synthesis mesoporous CuO/g-C_3N_4 heterostructures for highly enhanced and accelerated Hg(II) photoreduction under visible light. *J. Colloid Interface Sci.* **2020**, *580*, 223–233. [CrossRef]
97. Li, Q.; Yang, J.; Feng, D.; Wu, Z.; Wu, Q.; Park, S.S.; Ha, C.-S.; Zhao, D. Facile synthesis of porous carbon nitride spheres with hierarchical three-dimensional mesostructures for CO_2 capture. *Nano Res.* **2010**, *3*, 632–642. [CrossRef]
98. Zhang, J.; Zhang, M.; Yang, C.; Wang, X. Nanospherical Carbon Nitride Frameworks with Sharp Edges Accelerating Charge Collection and Separation at a Soft Photocatalytic Interface. *Adv. Mater.* **2014**, *26*, 4121–4126. [CrossRef]
99. Duan, Y.; Cao, Y.; Shang, X.; Jia, D.; Li, C. Synthesis of g-C_3N_4/W-SBA-15 Composites for Photocatalytic Degradation of Tetracycline Hydrochloride. *J. Inorg. Organomet. Polym. Mater.* **2021**, *31*, 2140–2149. [CrossRef]
100. Xu, J.; Chen, T.; Wang, X.; Xue, B.; Li, Y.X. Preparation of mesoporous graphitic carbon nitride using hexamethylenetetramine as a new precursor and catalytic application in the transesterification of beta-keto esters. *Catal. Sci. Technol.* **2014**, *4*, 2126–2133. [CrossRef]
101. Zhao, D.; Feng, J.; Huo, Q.; Melosh, N.; Fredrickson, G.H.; Chmelka, B.F.; Stucky, G.D. Triblock copolymer syntheses of mesoporous silica with periodic 50 to 300 angstrom pores. *Science* **1998**, *279*, 548–552. [CrossRef]
102. Chen, X.; Jun, Y.-S.; Takanabe, K.; Maeda, K.; Domen, K.; Fu, X.; Antonietti, M.; Wang, X. Ordered Mesoporous SBA-15 Type Graphitic Carbon Nitride: A Semiconductor Host Structure for Photocatalytic Hydrogen Evolution with Visible Light. *Chem. Mater.* **2009**, *21*, 4093–4095. [CrossRef]
103. Zhao, X.; Zhang, Y.; Li, F.; Wang, Y.; Pan, W.; Leung, D.Y.C. Salt-air Template Synthesis of Na and O Doped Porous Graphitic Carbon Nitride Nanorods with Exceptional Photocatalytic H_2 Evolution Activity. *Carbon* **2021**, *179*, 42–52. [CrossRef]
104. Tang, Q.; Niu, R.; Gong, J. Salt-Templated Synthesis of 3D Porous Foam-like C_3N_4 Towards High-Performance Photodegradation of Tetracyclines. *New J. Chem.* **2020**, *44*, 17405–17412. [CrossRef]
105. Chen, Z.; Lu, S.; Wu, Q.; He, F.; Zhao, N.; He, C.; Shi, C. Salt-assisted Synthesis of 3D Open Porous g-C_3N_4 Decorated with Cyano Groups for Photocatalytic Hydrogen Evolution. *Nanoscale* **2018**, *10*, 3008–3013. [CrossRef]
106. Jing, H.; You, M.; Yi, S.; Li, T.; Ji, H.; Wang, Y.; Zhang, Z.; Zhang, R.; Chen, D.; Yang, H. Precursor-Engineering Coupled Microwave Molten-Salt Strategy Enhances Photocatalytic Hydrogen Evolution Performance of g-C_3N_4 Nanostructures. *ChemSusChem* **2020**, *13*, 827–837. [CrossRef]
107. Gong, J.; Zhang, J.; Lin, H.; Yuan, J. "Cooking carbon in a solid salt": Synthesis of porous heteroatom-doped carbon foams for enhanced organic pollutant degradation under visible light. *Appl. Mater. Today* **2018**, *12*, 168–176. [CrossRef]
108. Sun, X.D.; Li, Y.Y.; Zhou, J.; Ma, C.H.; Wang, Y.; Zhu, J.H. Facile synthesis of high photocatalytic active porous g-C_3N_4 with $ZnCl_2$ template. *J. Colloid Interface Sci.* **2015**, *451*, 108–116. [CrossRef]
109. Yang, F.; Liu, D.; Li, Y.; Cheng, L.; Ye, J. Salt-Template-Assisted Construction of Honeycomb-Like Structured g-C_3N_4 with Tunable Band Structure for Enhanced Photocatalytic H_2 Production. *Appl. Catal. B Environ.* **2019**, *240*, 64–71. [CrossRef]
110. Fei, B.; Tang, Y.; Wang, X.; Dong, X.; Liang, J.; Fei, X.; Xu, L.; Song, Y.; Zhang, F. One-Pot Synthesis of Porous g-C_3N_4 Nanomaterials with Different Morphologies and Their Superior Photocatalytic Performance. *Mater. Res. Bull.* **2018**, *102*, 209–217. [CrossRef]
111. Wang, X.; Liu, Q.; Yang, Q.; Zhang, Z.; Fang, X. Three-Dimensional g-C_3N_4 Aggregates of Hollow Bubbles with High Photocatalytic Degradation of Tetracycline. *Carbon* **2018**, *136*, 103–112. [CrossRef]
112. Shahzeydi, A.; Ghiaci, M.; Farrokhpour, H.; Shahvar, A.; Sun, M.; Saraji, M. Facile and Green Synthesis of Copper Nanoparticles Loaded on the Amorphous Carbon Nitride for the Oxidation of Cyclohexane. *Chem. Eng. J.* **2019**, *370*, 1310–1321. [CrossRef]
113. Yang, H.; Lv, K.; Zhu, J.; Li, Q.; Tang, D.; Ho, W.; Li, M.; Carabineiro, S.A.C. Effect of Mesoporous g-C_3N_4 Substrate on Catalytic Oxidation of CO over Co_3O_4. *Appl. Surf. Sci.* **2017**, *401*, 333–340. [CrossRef]
114. Xu, J.; Jiang, D.; Qin, Y.; Xia, J.; Jiang, D.; Chen, H.-Y. C_3N_4 Nanosheet Modified Microwell Array with Enhanced Electrochemiluminescence for Total Analysis of Cholesterol at Single Cells. *Anal. Chem.* **2017**, *89*, 2216–2220. [CrossRef]
115. Ashrafi, H.; Akhond, M.; Absalan, G. Adsorption and Photocatalytic Degradation of Aqueous Methylene Blue Using Nanoporous Carbon Nitride. *J. Photochem. Photobiol. A Chem.* **2020**, *396*, 112533. [CrossRef]
116. Shawky, A.; Albukhari, S.M.; Amin, M.S.; Zaki, Z.I. Mesoporous V_2O_5/g-C_3N_4 Nanocomposites for Promoted Mercury (II) Ions Reduction Under Visible Light. *J. Inorg. Organomet. Polym. Mater.* **2021**, *31*, 4209–4221. [CrossRef]
117. Qi, K.; Cui, N.; Zhang, M.; Ma, Y.; Wang, G.; Zhao, Z.; Khataee, A. Ionic Liquid-Assisted Synthesis of Porous Boron-Doped Graphitic Carbon Nitride for Photocatalytic Hydrogen Production. *Chemosphere* **2021**, *272*, 129953. [CrossRef]
118. Li, P.; Liu, L.; An, W.; Wang, H.; Cui, W. Efficient Photothermal Catalytic CO_2 Reduction to CH_3CH_2OH over Cu_2O/g-C_3N_4 Assisted by Ionic Liquids. *Appl. Surf. Sci.* **2021**, *565*, 150448. [CrossRef]
119. Chen, F.; Huang, S.; Xu, Y.; Huang, L.; Wei, W.; Xu, H.; Li, H. Novel Ionic Liquid Modified Carbon Nitride Fabricated by in Situ Pyrolysis of 1-Butyl-3-Methylimidazolium Cyanamide to Improve Electronic Structure for Efficiently Degradation of Bisphenol A. *Colloid Surf. A Physicochem. Eng. Asp.* **2021**, *610*, 125648. [CrossRef]
120. Peer, M.; Lusardi, M.; Jensen, K.F. Facile Soft-Templated Synthesis of High-Surface Area and Highly Porous Carbon Nitrides. *Chem. Mater.* **2017**, *29*, 1496–1506. [CrossRef]

121. Gao, F.; Hu, J.; Peng, C.; Liu, H.; Hu, Y. Synergic Effects of Imidazolium Ionic Liquids on P123 Mixed Micelles for Inducing Micro/Mesoporous Materials. *Langmuir* **2012**, *28*, 2950–2959. [CrossRef] [PubMed]
122. Zhao, S.; Zhang, Y.; Wang, Y.; Zhou, Y.; Qiu, K.; Zhang, C.; Fang, J.; Sheng, X. Ionic Liquid-Assisted Synthesis of Br-Modified g-C_3N_4 Semiconductors with High Surface Area and Highly Porous Structure for Photoredox Water Splitting. *J. Power Sources* **2017**, *370*, 106–113. [CrossRef]
123. Yan, H. Soft-Templating Synthesis of Mesoporous Graphitic Carbon Nitride with Enhanced Photocatalytic H_2 Evolution under Visible Light. *Chem. Commun.* **2012**, *48*, 3430–3432. [CrossRef] [PubMed]
124. He, F.; Chen, G.; Zhou, Y.; Yu, Y.; Zheng, Y.; Hao, S. The Facile Synthesis of Mesoporous g-C_3N_4 with Highly Enhanced Photocatalytic H_2 Evolution Performance. *Chem. Commun.* **2015**, *51*, 16244–16246. [CrossRef] [PubMed]
125. Fan, H.; Wang, N.; Tian, Y.; Ai, S.; Zhan, J. Acetic Acid Induced Synthesis of Laminated Activated Carbon Nitride Nanostructures. *Carbon* **2016**, *107*, 747–753. [CrossRef]
126. Iqbal, W.; Dong, C.; Xing, M.; Tan, X.; Zhang, J. Eco-Friendly One-Pot Synthesis of Well-Adorned Mesoporous g-C_3N_4 with Efficiently Enhanced Visible Light Photocatalytic Activity. *Catal. Sci. Technol.* **2017**, *7*, 1726–1734. [CrossRef]
127. Chen, Y.; Li, W.; Jiang, D.; Men, K.; Li, Z.; Li, L.; Sun, S.; Li, J.; Huang, Z.-H.; Wang, L.-N. Facile Synthesis of Bimodal Macroporous g-C_3N_4/SnO_2 Nanohybrids with Enhanced Photocatalytic Activity. *Sci. Bull.* **2019**, *64*, 44–53. [CrossRef]
128. Li, G.; Shi, J.; Zhang, G.; Fang, Y.; Anpo, M.; Wang, X. The Facile Synthesis of Graphitic Carbon Nitride from Amino Acid and Urea for Photocatalytic H_2 Production. *Res. Chem. Intermed.* **2017**, *43*, 5137–5152. [CrossRef]
129. Ismael, M.; Wu, Y.; Taffa, D.H.; Bottke, P.; Wark, M. Graphitic Carbon Nitride Synthesized by Simple Pyrolysis: Role of Precursor in Photocatalytic Hydrogen Production. *New J. Chem.* **2019**, *43*, 6909–6920. [CrossRef]
130. Zhang, J.; Chen, X.; Takanabe, K.; Maeda, K.; Domen, K.; Epping, J.D.; Fu, X.; Antonietti, M.; Wang, X. Synthesis of a Carbon Nitride Structure for Visible-Light Catalysis by Copolymerization. *Angew. Chem. Int. Ed.* **2010**, *49*, 441–444. [CrossRef]
131. Zhang, J.; Zhang, G.; Chen, X.; Lin, S.; Moehlmann, L.; Dolega, G.; Lipner, G.; Antonietti, M.; Blechert, S.; Wang, X. Co-Monomer Control of Carbon Nitride Semiconductors to Optimize Hydrogen Evolution with Visible Light. *Angew. Chem. Int. Ed.* **2012**, *51*, 3183–3187. [CrossRef]
132. Segura, J.L.; Mancheño, M.J.; Zamora, F. Covalent organic frameworks based on Schiff-base chemistry: Synthesis, properties and potential applications. *Chem. Soc. Rev.* **2016**, *45*, 5635–5671. [CrossRef]
133. Xu, J.; Li, Y.; Peng, S.; Lu, G.; Li, S. Eosin Y-Sensitized Graphitic Carbon Nitride Fabricated by Heating Urea for Visible Light Photocatalytic Hydrogen Evolution: The Effect of the Pyrolysis Temperature of Urea. *Phys. Chem. Chem. Phys.* **2013**, *15*, 7657–7665. [CrossRef]
134. Zhang, M.; Xu, J.; Zong, R.; Zhu, Y. Enhancement of Visible Light Photocatalytic Activities via Porous Structure of g-C_3N_4. *Appl. Catal. B Environ.* **2014**, *147*, 229–235. [CrossRef]
135. Huang, H.; Xiao, K.; Tian, N.; Dong, F.; Zhang, T.; Du, X.; Zhang, Y. Template-Free Precursor-Surface-Etching Route to Porous, Thin g-C_3N_4 Nanosheets for Enhancing Photocatalytic Reduction and Oxidation Activity. *J. Mater. Chem. A* **2017**, *5*, 17452–17463. [CrossRef]
136. Xu, J.; Wang, Y.; Zhu, Y. Nanoporous Graphitic Carbon Nitride with Enhanced Photocatalytic Performance. *Langmuir* **2013**, *29*, 10566–10572. [CrossRef]
137. Bai, J.; Yin, C.; Xu, H.; Chen, G.; Ni, Z.; Wang, Z.; Li, Y.; Kang, S.; Zheng, Z.; Li, X. Facile Urea-assisted Precursor Pre-treatment to Fabricate Porous g-C_3N_4 Nanosheets for Remarkably Enhanced Visible-light-driven Hydrogen Evolution. *J. Colloid Interface Sci.* **2018**, *532*, 280–286. [CrossRef]
138. Liang, L.; Cong, Y.; Wang, F.; Yao, L.; Shi, L. Hydrothermal Pre-Treatment induced Cyanamide to Prepare Porous g-C_3N_4 with Boosted Photocatalytic Performance. *Diam. Relat. Mater.* **2019**, *98*, 107499. [CrossRef]
139. Butt, F.K.; Hauenstein, P.; Kosiahn, M.; Garlyyev, B.; Dao, M.; Lang, A.; Scieszka, D.; Liang, Y.; Kreuzpaintner, W. An Innovative Microwave-Assisted Method for the Synthesis of Mesoporous Two Dimensional g-C_3N_4: A Revisited Insight into a Potential Electrode Material for Supercapacitors. *Microporous Mesoporous Mater.* **2020**, *294*, 109853. [CrossRef]
140. Wang, L.; Hong, Y.; Liu, E.; Duan, X.; Lin, X.; Shi, J. A bottom-up acidification strategy engineered ultrathin g-C3N4 nanosheets towards boosting photocatalytic hydrogen evolution. *Carbon* **2020**, *163*, 234–243. [CrossRef]
141. Shen, J.; Yang, H.; Shen, Q.; Feng, Y.; Cai, Q.; Yang, H. Template-Free Synthesis of Three-Dimensional Nanoporous Bulk Graphitic Carbon Nitride with Remarkably Enhanced Photocatalytic Activity and Good Separation Properties. *Eur. J. Inorg. Chem.* **2015**, *2015*, 2611–2618. [CrossRef]
142. Li, B.; Si, Y.; Fang, Q.; Shi, Y.; Huang, W.-Q.; Hu, W.; Pan, A.; Fan, X.; Huang, G.-F. Hierarchical Self-assembly of Well-Defined Louver-Like P-Doped Carbon Nitride Nanowire Arrays with Highly Efficient Hydrogen Evolution. *Nano-Micro Lett.* **2020**, *12*, 52. [CrossRef] [PubMed]
143. Dong, G.; Zhang, L. Porous Structure Dependent Photoreactivity of Graphitic Carbon Nitride under Visible Light. *J. Mater. Chem.* **2012**, *22*, 1160–1166. [CrossRef]
144. Zhang, X.-S.; Hu, J.-Y.; Jiang, H. Facile Modification of a Graphitic Carbon Nitride Catalyst to Improve Its Photoreactivity under Visible Light Irradiation. *Chem. Eng. J.* **2014**, *256*, 230–237. [CrossRef]
145. Xie, L.; Ding, Y.; Wang, X.; Xu, W. Chlorine-Assisted Fabrication of Hybrid Supramolecular Structures via Electrostatic Interactions. *Phys. Chem. Chem. Phys.* **2019**, *21*, 9357–9361. [CrossRef]

146. Shen, B.; Hong, Z.; Chen, Y.; Lin, B.; Gao, B. Template-Free Synthesis of a Novel Porous g-C_3N_4 with 3D Hierarchical Structure for Enhanced Photocatalytic H_2 Evolution. *Mater. Lett.* **2014**, *118*, 208–211. [CrossRef]
147. Liao, Y.; Zhu, S.; Ma, J.; Sun, Z.; Yin, C.; Zhu, C.; Lou, X.; Zhang, D. Tailoring the Morphology of g-C_3N_4 by Self-Assembly towards High Photocatalytic Performance. *ChemCatChem* **2014**, *6*, 3419–3425. [CrossRef]
148. Wang, X.; Zhou, C.; Shi, R.; Liu, Q.; Waterhouse, G.I.N.; Wu, L.; Tung, C.-H.; Zhang, T. Supramolecular Precursor Strategy for the Synthesis of Holey Graphitic Carbon Nitride Nanotubes with Enhanced Photocatalytic Hydrogen Evolution Performance. *Nano Res.* **2019**, *12*, 2385–2389. [CrossRef]
149. Wu, M.; Gong, Y.; Nie, T.; Zhang, J.; Wang, R.; Wang, H.; He, B. Template-free synthesis of nanocage-like g-C_3N_4 with high surface area and nitrogen defects for enhanced photocatalytic H_2 activity. *J. Mater. Chem. A* **2019**, *7*, 5324–5332. [CrossRef]
150. Zhu, B.; Xu, G.; Li, X.; Wang, Z.; Lv, J.; Shu, X.; Huang, J.; Zheng, Z.; Wu, Y. Ultrathin Porous g-CN Nanosheets Fabricated by Direct Calcination of Pre-Treated Melamine for Enhanced Photocatalytic Performance. *J. Mater. Res.* **2019**, *34*, 3462–3473. [CrossRef]
151. Piradashvili, K.; Alexandrino, E.M.; Wurm, F.R.; Landfester, K. Reactions and Polymerizations at the Liquid–Liquid Interface. *Chem. Rev.* **2016**, *116*, 2141–2169. [CrossRef]
152. Qin, B.; Zhang, S.; Song, Q.; Huang, Z.; Xu, J.-F.; Zhang, X. Supramolecular Interfacial Polymerization: A Controllable Method of Fabricating Supramolecular Polymeric Materials. *Angew. Chem. Int. Ed.* **2017**, *56*, 7639–7643. [CrossRef]
153. Dolai, S.; Karjule, N.; Azoulay, A.; Barrio, J. Monomer sequence design at two solvent interface enables the synthesis of highly photoactive carbon nitride. *RSC Adv.* **2019**, *9*, 26091–26096. [CrossRef]
154. Dolai, S.; Barrio, J.; Peng, G.; Grafmüller, A.; Shalom, M. Tailoring carbon nitride properties and photoactivity by interfacial engineering of hydrogen-bonded frameworks. *Nanoscale* **2019**, *11*, 5564–5570. [CrossRef]
155. Azoulay, A.; Barrio, J.; Shalom, M. Modifying Crystallinity, Morphology, and Photophysical Properties of Carbon Nitride by Using Crystals as Reactants. *Isr. J. Chem.* **2020**, *60*, 544–549. [CrossRef]
156. Barrio, J.; Barzilai, S.; Karjule, N.; Amo-Ochoa, P.; Zamora, F.; Shalom, M. Synergistic Doping and Surface Decoration of Carbon Nitride Macrostructures by Single Crystal Design. *ACS Appl. Energy Mater.* **2021**, *4*, 1868–1875. [CrossRef]
157. Barrio, J.; Lin, L.; Amo-Ochoa, P.; Tzadikov, J.; Peng, G.; Sun, J.; Zamora, F.; Wang, X.; Shalom, M. Unprecedented Centimeter-Long Carbon Nitride Needles: Synthesis, Characterization and Applications. *Small* **2018**, *14*, 1800633. [CrossRef]
158. Barrio, J.; Barzilai, S.; Karjule, N.; Amo-Ochoa, P.; Zamora, F.; Shalom, M. Fluorescent Carbon Nitride Macrostructures Derived from Triazine-Based Cocrystals. *Adv. Opt. Mater.* **2021**, *9*, 2100683. [CrossRef]
159. Fang, X.; Gao, R.; Yang, Y.; Yan, D. A Cocrystal Precursor Strategy for Carbon-Rich Graphitic Carbon Nitride toward High-Efficiency Photocatalytic Overall Water Splitting. *iScience* **2019**, *16*, 22–30. [CrossRef]
160. Gao, J.; Wang, J.; Qian, X.; Dong, Y.; Xu, H.; Song, R.; Yan, C.; Zhu, H.; Zhong, Q.; Qian, G.; et al. One-pot synthesis of copper-doped graphitic carbon nitride nanosheet by heating Cu-melamine supramolecular network and its enhanced visible-light-driven photocatalysis. *J. Solid State Chem.* **2015**, *228*, 60–64. [CrossRef]
161. Zhu, J.-N.; Zhu, X.-Q.; Cheng, F.-F.; Li, P.; Wang, F.; Xiao, Y.-W.; Xiong, W.-W. Preparing copper doped carbon nitride from melamine templated crystalline copper chloride for Fenton-like catalysis. *Appl. Catal. B Environ.* **2019**, *256*, 117830. [CrossRef]
162. Jiang, Z.; Zhang, X.; Chen, H.-S.; Hu, X.; Yang, P. Formation of g-C_3N_4 Nanotubes towards Superior Photocatalysis Performance. *ChemCatChem* **2019**, *11*, 4558–4567. [CrossRef]
163. Wang, J.; Xu, H.; Qian, X.; Dong, Y.; Gao, J.; Qian, G.; Yao, J. Direct Synthesis of Porous Nanorod-Type Graphitic Carbon Nitride/CuO Composite from Cu-Melamine Supramolecular Framework towards Enhanced Photocatalytic Performance. *Chem. Asian J.* **2015**, *10*, 1276–1280. [CrossRef]
164. Zhang, B.; Wang, Q.; Zhuang, J.; Guan, S.; Li, B. Molten Salt Assisted In-Situ Synthesis of TiO_2/g-C_3N_4 Composites with Enhanced Visible-Light-Driven Photocatalytic Activity and Adsorption Ability. *J. Photochem. Photobiol. A Chem.* **2018**, *362*, 1–13. [CrossRef]
165. Dong, F.; Li, Y.; Wang, Z.; Ho, W.-K. Enhanced Visible Light Photocatalytic Activity and Oxidation Ability of Porous Graphene-Like g-C_3N_4 Nanosheets via Thermal Exfoliation. *Appl. Surf. Sci.* **2015**, *358*, 393–403. [CrossRef]
166. Nicolosi, V.; Chhowalla, M.; Kanatzidis, M.G.; Strano, M.S.; Coleman, J.N. Liquid Exfoliation of Layered Materials. *Science* **2013**, *340*, 1226419. [CrossRef]
167. Ma, L.; Fan, H.; Wang, J.; Zhao, Y.; Tian, H.; Dong, G. Water-Assisted Ions In Situ Intercalation for Porous Polymeric Graphitic Carbon Nitride Nanosheets with Superior Photocatalytic Hydrogen Evolution Performance. *Appl. Catal. B Environ.* **2016**, *190*, 93–102. [CrossRef]
168. Liu, Y.; Shen, S.; Li, Z.; Ma, D.; Xu, G.; Fang, B. Mesoporous g-C_3N_4 Nanosheets with Improved Photocatalytic Performance for Hydrogen Evolution. *Mater. Charact.* **2021**, *174*, 111031. [CrossRef]
169. Zhang, X.; Wang, H.; Wang, H.; Zhang, Q.; Xie, J.; Tian, Y.; Wang, J.; Xie, Y. Single-Layered Graphitic-C_3N_4 Quantum Dots for Two-Photon Fluorescence Imaging of Cellular Nucleus. *Adv. Mater.* **2014**, *26*, 4438–4443. [CrossRef]
170. Guo, S.; Zhu, Y.; Yan, Y.; Min, Y.; Fan, J.; Xu, Q. Holey Structured Graphitic Carbon Nitride Thin Sheets with Edge Oxygen Doping via Photo-Fenton Reaction with Enhanced Photocatalytic Activity. *Appl. Catal. B Environ.* **2016**, *185*, 315–321. [CrossRef]
171. Yang, Z.; Xing, Z.; Feng, Q.; Jiang, H.; Zhang, J.; Xiao, Y.; Li, Z.; Chen, P.; Zhou, W. Sandwich-Like Mesoporous Graphite-Like Carbon Nitride (Meso-g-C_3N_4)/WP/Meso-g-C_3N_4 Laminated Heterojunctions Solar-Driven Photocatalysts. *J. Colloid Interface Sci.* **2020**, *568*, 255–263. [CrossRef] [PubMed]

172. Zhang, S.; Hu, C.; Ji, H.; Zhang, L.; Li, F. Facile Synthesis of Nitrogen-Deficient Mesoporous Graphitic Carbon Nitride for Highly Efficient Photocatalytic Performance. *Appl. Surf. Sci.* **2019**, *478*, 304–312. [CrossRef]
173. Wu, W.; Li, X.; Ruan, Z.; Li, Y.; Xu, X.; Yuan, Y.; Lin, K. Fabrication of a TiO_2 trapped meso/macroporous g-C_3N_4 heterojunction photocatalyst and understanding its enhanced photocatalytic activity based on optical simulation analysis. *Inorg. Chem. Front.* **2018**, *5*, 481–489. [CrossRef]
174. Xu, J.; Shen, K.; Xue, B.; Li, Y.-X.; Cao, Y. Synthesis of Three-Dimensional Mesostructured Graphitic Carbon Nitride Materials and their Application as Heterogeneous Catalysts for Knoevenagel Condensation Reactions. *Catal. Lett.* **2013**, *143*, 600–609. [CrossRef]
175. Wu, X.; Ma, H.; Zhong, W.; Fan, J.; Yu, H. Porous Crystalline g-C_3N_4: Bifunctional $NaHCO_3$ Template-Mediated Synthesis and Improved Photocatalytic H_2 Evolution Rate. *Appl. Catal. B Environ.* **2020**, *271*, 118899. [CrossRef]
176. Tang, J.; Zhang, Q.; Liu, Y.; Liu, Y.; Wang, K.; Xu, N.; Yu, L.; Tong, Q.; Fan, Y. The Photocatalytic Redox Properties of Polymeric Carbon Nitride Nanocages (PCNCs) with Mesoporous Hollow Spherical Structures Prepared by a ZnO-Template Method. *Microporous Mesoporous Mater.* **2020**, *292*, 109639. [CrossRef]
177. Zhao, S.; Fang, J.; Wang, Y.; Zhang, Y.; Zhou, Y.; Zhuo, S. Construction of Three-Dimensional Mesoporous Carbon Nitride with High Surface area for Efficient Visible-Light-Driven Hydrogen Evolution. *J. Colloid Interface Sci.* **2020**, *561*, 601–608. [CrossRef]
178. Wang, C.; Zhang, G.; Zhang, H.; Li, Z.; Wen, Y. One-Pot Synthesis of Porous g-C_3N_4 Nanosheets with Enhanced Photocatalytic Activity under Visible Light. *Diam. Relat. Mater.* **2021**, *116*, 108416. [CrossRef]
179. Fei, T.; Qin, C.; Zhang, Y.; Dong, G.; Wang, Y.; Zhou, Y.; Cui, M. A 3D Peony-Like Sulfur-Doped Carbon Nitride Synthesized by Self-Assembly for Efficient Photocatalytic Hydrogen Production. *Int. J. Hydrog. Energy* **2021**, *46*, 20481–20491. [CrossRef]
180. She, X.; Liu, L.; Ji, H.; Mo, Z.; Li, Y.; Huang, L.; Du, D.; Xu, H.; Li, H. Template-Free Synthesis of 2D Porous Ultrathin Nonmetal-Doped g-C3N4 Nanosheets with Highly Efficient Photocatalytic H_2 Evolution from Water Under Visible Light. *Appl. Catal. B Environ.* **2016**, *187*, 144–153. [CrossRef]
181. Xu, J.; Wang, Z.; Zhu, Y. Enhanced Visible-Light-Driven Photocatalytic Disinfection Performance and Organic Pollutant Degradation Activity of Porous g-C_3N_4 Nanosheets. *ACS Appl. Mater. Interfaces* **2017**, *9*, 27727–27735. [CrossRef]
182. Mei, Z.; Wang, G.; Yan, S.; Wang, J. Rapid Microwave-Assisted Synthesis of 2D/1D $ZnIn_2S_4$/TiO_2 S-Scheme Heterojunction for Catalyzing Photocatalytic Hydrogen Evolution. *Acta Phys. Chim. Sin.* **2021**, *37*, 2009097. [CrossRef]
183. Wu, M.; Zhang, J.; He, B.-B.; Wang, H.-W.; Wang, R.; Gong, Y.-S. In-Situ Construction of Coral-Like Porous P-Doped g-C_3N_4 Tubes with Hybrid 1D/2D Architecture and High Efficient Photocatalytic Hydrogen Evolution. *Appl. Catal. B Environ.* **2019**, *241*, 159–166. [CrossRef]
184. Zhang, Y.; Chen, Z.; Li, J.; Lu, Z.; Wang, X. Self-Assembled Synthesis of Oxygen-Doped g-C_3N_4 Nanotubes in Enhancement of Visible-Light Photocatalytic Hydrogen. *J. Energy Chem.* **2021**, *54*, 36–44. [CrossRef]
185. Malik, R.; Tomer, V.K. State-of-the-Art Review of Morphological Advancements in Graphitic Carbon Nitride (g-CN) for Sustainable Hydrogen Production. *Renew. Sustain. Energy Rev.* **2021**, *135*, 110235. [CrossRef]
186. Wang, J.; Wang, G.; Wang, X.; Wu, Y.; Su, Y.; Tang, H. 3D/2D Direct Z-Scheme Heterojunctions of Hierarchical TiO_2 Microflowers/g-C_3N_4 Nanosheets with Enhanced Charge Carrier Separation for Photocatalytic H_2 Evolution. *Carbon* **2019**, *149*, 618–626. [CrossRef]
187. Xu, H.; Xiao, R.; Huang, J.; Jiang, Y.; Zhao, C.; Yang, X. In Situ Construction of Protonated g-C_3N_4/Ti_3C_2 MXene Schottky Heterojunctions for Efficient Photocatalytic Hydrogen Production. *Chin. J. Catal.* **2021**, *42*, 107–114. [CrossRef]
188. Ye, R.; Fang, H.; Zheng, Y.-Z.; Li, N.; Wang, Y.; Tao, X. Fabrication of $CoTiO_3$/g-C_3N_4 Hybrid Photocatalysts with Enhanced H_2 Evolution: Z-Scheme Photocatalytic Mechanism Insight. *ACS Appl. Mater. Interfaces* **2016**, *8*, 13879–13889. [CrossRef]
189. Chen, X.; Shi, R.; Chen, Q.; Zhang, Z.; Jiang, W.; Zhu, Y.; Zhang, T. Three-Dimensional Porous g-C_3N_4 for Highly Efficient Photocatalytic Overall Water Splitting. *Nano Energy* **2019**, *59*, 644–650. [CrossRef]
190. Liu, Q.; Shen, J.; Yang, X.; Zhang, T.; Tang, H. 3D Reduced Graphene Oxide Aerogel-Mediated Z-Scheme Photocatalytic System for Highly Efficient Solar-Driven Water Oxidation and Removal of Antibiotics. *Appl. Catal. B Environ.* **2018**, *232*, 562–573. [CrossRef]
191. Wang, J.; Wang, G.; Jiang, J.; Wan, Z.; Su, Y.; Tang, H. Insight into Charge Carrier Separation and Solar-Light Utilization: rGO Decorated 3D ZnO Hollow Microspheres for Enhanced Photocatalytic Hydrogen Evolution. *J. Colloid Interface Sci.* **2020**, *564*, 322–332. [CrossRef]
192. Wen, P.; Sun, Y.; Li, H.; Liang, Z.; Wu, H.; Zhang, J.; Zeng, H.; Geyer, S.M.; Jiang, L. A Highly Ective Three-Dimensional Z-Scheme ZnO/Au/g-C_3N_4 Photocathode for Efficient Photoelectrochemical Water Splitting. *Appl. Catal. B Environ.* **2020**, *263*, 118180. [CrossRef]
193. Niu, H.; Zhao, W.; Lv, H.; Yang, Y.; Cai, Y. Accurate Design of Hollow/Tubular Porous g-C_3N_4 from Melamine-Cyanuric Acid Supramolecular Prepared with Mechanochemical Method. *Chem. Eng. J.* **2021**, *411*, 128400. [CrossRef]
194. Wang, T.; Meng, X.; Li, P.; Ouyang, S.; Chang, K.; Liu, G.; Mei, Z.; Ye, J. Photoreduction of CO_2 over the Well-Crystallized Ordered Mesoporous TiO_2 with the Confined Space Effect. *Nano Energy* **2014**, *9*, 50–60. [CrossRef]
195. Elbanna, O.; Fujitsuka, M.; Majima, T. g-C_3N_4/TiO_2 Mesocrystals Composite for H_2 Evolution under Visible-Light Irradiation and Its Charge Carrier Dynamics. *ACS Appl. Mater. Interfaces* **2017**, *9*, 34844–34854. [CrossRef]
196. Niu, P.; Yin, L.-C.; Yang, Y.-Q.; Liu, G.; Cheng, H.-M. Increasing the Visible Light Absorption of Graphitic Carbon Nitride (Melon) Photocatalysts by Homogeneous Self-Modification with Nitrogen Vacancies. *Adv. Mater.* **2014**, *26*, 8046–8052. [CrossRef]
197. Liang, Q.; Li, Z.; Huang, Z.-H.; Kang, F.; Yang, Q.-H. Holey Graphitic Carbon Nitride Nanosheets with Carbon Vacancies for Highly Improved Photocatalytic Hydrogen Production. *Adv. Funct. Mater.* **2015**, *25*, 6885–6892. [CrossRef]

198. Tu, W.; Xu, Y.; Wang, J.; Zhang, B.; Zhou, T.; Yin, S.; Wu, S.; Li, C.; Huang, Y.; Zhou, Y.; et al. Investigating the Role of Tunable Nitrogen Vacancies in Graphitic Carbon Nitride Nanosheets for Efficient Visible-Light-Driven H_2 Evolution and CO_2 Reduction. *ACS Sustain. Chem. Eng.* **2017**, *5*, 7260–7268. [CrossRef]
199. Sagara, N.; Kamimura, S.; Tsubota, T.; Ohno, T. Photoelectrochemical CO_2 Reduction by a P-Type Boron-Doped g-C_3N_4 Electrode under Visible Light. *Appl. Catal. B Environ.* **2016**, *192*, 193–198. [CrossRef]
200. Arumugam, M.; Tahir, M.; Praserthdam, P. Effect of Nonmetals (B, O, P, and S) Doped with Porous g-C_3N_4 for Improved Electron Transfer Towards Photocatalytic CO_2 Reduction with Water into CH_4. *Chemosphere* **2022**, *286*, 131765. [CrossRef]
201. Wang, Y.; Tian, Y.; Yan, L.; Su, Z. DFT Study on Sulfur-Doped g-C_3N_4 Nanosheets as a Photocatalyst for CO_2 Reduction Reaction. *J. Phys. Chem. C* **2018**, *122*, 7712–7719. [CrossRef]
202. Wang, K.; Li, Q.; Liu, B.; Cheng, B.; Ho, W.; Yu, J. Sulfur-Doped g-C_3N_4 with Enhanced Photocatalytic CO_2-Reduction Performance. *Appl. Catal. B Environ.* **2015**, *176*, 44–52. [CrossRef]
203. Fu, J.; Zhu, B.; Jiang, C.; Cheng, B.; You, W.; Yu, J. Hierarchical Porous O-Doped g-C_3N_4 with Enhanced Photocatalytic CO_2 Reduction Activity. *Small* **2017**, *13*, 1603938. [CrossRef] [PubMed]
204. Lu, S.; Li, C.; Li, H.H.; Zhao, Y.F.; Gong, Y.Y.; Niu, L.Y.; Liu, X.J.; Wang, T. The Effects of Nonmetal Dopants on the Electronic, Optical and Chemical Performances of Monolayer g-C_3N_4 by First-Principles Study. *Appl. Surf. Sci.* **2017**, *392*, 966–974. [CrossRef]
205. Liao, G.; Gong, Y.; Zhang, L.; Gao, H.; Yang, G.-J.; Fang, B. Semiconductor Polymeric Graphitic Carbon Nitride Photocatalysts: The "Holy Grail" for Photocatalytic Hydrogen Evolution Reaction under Visible Light. *Energy Environ. Sci.* **2019**, *12*, 2080–2147. [CrossRef]
206. Liu, B.; Ye, L.; Wang, R.; Yang, J.; Zhang, Y.; Guan, R.; Tian, L.; Chen, X. Phosphorus-Doped Graphitic Carbon Nitride Nanotubes with Amino-rich Surface for Efficient CO_2 Capture, Enhanced Photocatalytic Activity, and Product Selectivity. *ACS Appl. Mater. Interfaces* **2018**, *10*, 4001–4009. [CrossRef]
207. Wang, Y.; Guo, L.; Zeng, Y.; Guo, H.; Wan, S.; Ou, M.; Zhang, S.; Zhong, Q. Amino-Assisted NH_2-UiO-66 Anchored on Porous g-C_3N_4 for Enhanced Visible-Light-Driven CO_2 Reduction. *ACS Appl. Mater. Interfaces* **2019**, *11*, 30673–30681. [CrossRef]
208. Moniz, S.J.A.; Shevlin, S.A.; Martin, D.J.; Guo, Z.-X.; Tang, J. Visible-Light Driven Heterojunction Photocatalysts for Water Splitting—A Critical Review. *Energy Environ. Sci.* **2015**, *8*, 731–759. [CrossRef]
209. Zhang, P.; Song, T.; Wang, T.; Zeng, H. Effectively Extending Visible Light Absorption with a Broad Spectrum Sensitizer for Improving the H_2 Evolution of In-Situ Cu/g-C_3N_4 Nanocomponents. *Int. J. Hydrog. Energy* **2017**, *42*, 14511–14521. [CrossRef]
210. Shi, L.; Wang, T.; Zhang, H.; Chang, K.; Ye, J. Electrostatic Self-Assembly of Nanosized Carbon Nitride Nanosheet onto a Zirconium Metal-Organic Framework for Enhanced Photocatalytic CO_2 Reduction. *Adv. Funct. Mater.* **2015**, *25*, 5360–5367. [CrossRef]
211. Wang, S.; He, F.; Zhao, X.; Zhang, J.; Ao, Z.; Wu, H.; Yin, Y.; Shi, L.; Xu, X.; Zhao, C.; et al. Phosphorous Doped Carbon Nitride Nanobelts for Photodegradation of Emerging Contaminants and Hydrogen Evolution. *Appl. Catal. B Environ.* **2019**, *257*, 117931. [CrossRef]
212. Wang, H.; Zhang, X.; Xie, Y. Photoresponsive Polymeric Carbon Nitride-Based Materials: Design and Application. *Mater. Today* **2019**, *23*, 72–86. [CrossRef]
213. Huang, J.; Ho, W.; Wang, X. Metal-Free Disinfection Effects Induced by Graphitic Carbon Nitride Polymers under Visible Light Illumination. *Chem. Commun.* **2014**, *50*, 4338–4340. [CrossRef]
214. Cao, S.; Low, J.; Yu, J.; Jaroniec, M. Polymeric Photocatalysts Based on Graphitic Carbon Nitride. *Adv. Mater.* **2015**, *27*, 2150–2176. [CrossRef]
215. Wang, X.; Liang, Y.; An, W.; Hu, J.; Zhu, Y.; Cui, W. Removal of Chromium (VI) by a Self-Regenerating and Metal free g-C_3N_4/Fraphene Hydrogel System via the Synergy of Adsorption and Photo-catalysis under Visible Light. *Appl. Catal. B Environ.* **2017**, *219*, 53–62. [CrossRef]
216. Zhao, J.; Li, B.; Liu, Z.; Dai, D.; Li, Y.; Shi, R.; Zhang, H. A Novel Solar-Triggered MIL-125(Ti)/g-C_3N_4/SA Composite Aerogel with High Catalytic Activity for Degradation of Organic Contaminants. *Sep. Purif. Technol.* **2021**, *279*, 119696. [CrossRef]
217. Zhang, M.; Jiang, W.; Liu, D.; Wang, J.; Liu, Y.; Zhu, Y.; Zhu, Y. Photodegradation of Phenol via C_3N_4-Agar Hybrid Hydrogel 3D Photocatalysts with Free Separation. *Appl. Catal. B Environ.* **2016**, *183*, 263–268. [CrossRef]
218. Huang, Q.; Wang, C.; Hao, D.; Wei, W.; Wang, L.; Ni, B.-J. Ultralight Biodegradable 3D-g-C_3N_4 Aerogel for Advanced Oxidation Water Treatment Driven by Oxygen Delivery Channels and Triphase Interfaces. *J. Clean. Prod.* **2021**, *288*, 125091. [CrossRef]
219. Lv, Y.; Liu, H.; Jin, D.; Yang, H.; He, D.; Zhang, Z.; Zhang, Y.; Qu, J.; Zhang, Y.-N. Effective Degradation of Norfloxacin on Ag_3PO_4/CNTs Photoanode: Z-Scheme Mechanism, Reaction Pathway, and Toxicity Assessment. *Chem. Eng. J.* **2022**, *429*, 132092. [CrossRef]
220. Liu, S.; Jiang, X.; Waterhouse, G.I.N.; Zhang, Z.-M.; Yu, L.-M. Efficient Photoelectrocatalytic Degradation of Azo-Dyes over Polypyrrole/Titanium Oxide/Reduced Graphene Oxide Electrodes under Visible Light: Performance Evaluation and Mechanism Insights. *Chemosphere* **2022**, *288*, 132509. [CrossRef]
221. Liang, F.; Zhu, Y. Enhancement of Mineralization Ability for Phenol via Synergetic Effect of Photoelectrocatalysis of *g*-C_3N_4 Film. *Appl. Catal. B Environ.* **2016**, *180*, 324–329. [CrossRef]
222. Qi, F.; Yang, B.; Wang, Y.; Mao, R.; Zhao, X. H_2O_2 Assisted Photoelectrocatalytic Oxidation of Ag-Cyanide Complexes at Metal-free *g*-C_3N_4 Photoanode with Simultaneous Ag Recovery. *ACS Sustain. Chem. Eng.* **2017**, *5*, 5001–5007. [CrossRef]
223. Qiao, M.; Wu, X.; Zhao, S.; Djellabi, R.; Zhao, X. Peroxymonosulfate Enhanced Photocatalytic Decomposition of Silver-Cyanide Complexes Using *g*-C_3N_4 Nanosheets with Simultaneous Recovery of Silver. *Appl. Catal. B Environ.* **2020**, *265*, 118587. [CrossRef]

224. Zhao, X.; Pan, D.; Chen, X.; Li, R.; Jiang, T.; Wang, W.; Li, G.; Leung, D.Y.C. *g*-C_3N_4 Photoanode for Photoelectrocatalytic Synergistic Pollutant Degradation and Hydrogen Evolution. *Appl. Surf. Sci.* **2019**, *467-468*, 658–665. [CrossRef]
225. Wu, L.; Li, F.; Xu, Y.; Zhang, J.W.; Zhang, D.; Li, G.; Li, H. Plasmon-Induced Photoelectrocatalytic Activity of Au Nanoparticles Enhanced TiO_2 Nanotube Arrays Electrodes for Environmental Remediation. *Appl. Catal. B Environ.* **2015**, *164*, 217–224. [CrossRef]